This is a preprint, the final version is subject to change, of the American Mineralogist (MSA)
Cite as Authors (Year) Title. American Mineralogist, in press.
(DOI will not work until issue is live.) DOI: http://dx.doi.org/10.2138/am.2013.4333

Fundamental Mössbauer Parameters of Synthetic Ca-Mg-Fe Pyroxenes

M. DARBY DYAR[1], RACHEL L. KLIMA[2], ALEXANDRA FLEAGLE[1], AND SAMANTHA E. PEEL[1]

[1]Department of Astronomy, Mount Holyoke College, 50 College St., South Hadley, MA 01075

[2]Johns Hopkins University, Applied Physics Laboratory, Laurel, MD 20723

Revision 1

Keywords: Mössbauer, recoil-free fraction, orthopyroxene, clinopyroxene, hedenbergite, diopside, pigeonite, enstatite, ferrosilite, augite

ABSTRACT

Understanding of Fe site occupancy across the Ca-Fe-Mg pyroxene quadrilateral requires knowledge of space group and appreciation of the diversity of site geometries across Ca-Mg-Fe composition space. Most commonly, these site occupancies are measured using some combination of single crystal structure refinements (SREF) from x-ray diffraction data and Mössbauer spectroscopy for bulk measurements. The vast majority of previous Mössbauer studies have been hampered by the lack of differential recoil-free fraction data that describe how the Fe^{2+} and Fe^{3+} cations are bonded in the M1 and M2 sites in pyroxene. To remedy this situation, this paper examines 658 Mössbauer spectra acquired from 64 synthetic samples covering the pyroxene quadrilateral in roughly 10 mol.% increments, and determines their fundamental Mössbauer parameters as a function of composition. Results show variations in all the Mössbauer parameters studied: center shift (δ), quadrupole splitting (Δ), area, recoil-free fraction (f), Mössbauer temperature (Θ_M), and intrinsic isomer shift (δ_I). The most systematic variations with composition are seen for δ and f, while small variations are seen for Δ, Θ_M, and δ_I. These data are then related to characteristics of the pyroxene crystal structure to examine the relationship between site geometry and recoil-free fraction. In general, smaller bond lengths (e.g., in the M1 site along the enstatite-ferrosilite join) result in higher f values. As Ca is added to the structure and Mg is removed, the f value for M1 increases as the site becomes larger and more regular. Larger sites with lower bond strengths result in lower values of f because the cation is less tightly bound in the crystal structure and thus encounters more recoil. This result is in keeping with theoretical expectations, but has not previously been clearly demonstrated for minerals with experimental data. Values of recoil-free fraction determined in this study will

42 facilitate more accurate determinations of cation site occupancies in pyroxenes from Mössbauer
43 data and lend insights into the geometries of the M1 and M2 sites.
44

INTRODUCTION

The technique of Mössbauer spectroscopy is now more than 50 years old, and it has become the standard method for determination of the valence state and site occupancy of iron in minerals. In recent years, the field of petrology has become more dependent on microanalytical techniques, and the large sample quantities needed for conventional analyses have made Mössbauer spectroscopy difficult to apply to the study of rock-forming minerals in geologically-significant parageneses. Now, improvements in both the instrumentation (McCammon 1994) for and the modeling (Dyar et al. 2006) of Mössbauer spectra have opened up the possibilities for analysis of a much broader range of materials than ever before. Both low-Fe materials and small sample quantities can now be studied successfully. These advances have the potential to turn the interest of the scientific community once again to the study of Fe^{3+} and Fe^{2+} partitioning in a wide variety of geological materials.

To prepare this field for the next 50 years (and beyond), we have undertaken a long-term set of experiments designed to generate fundamental data that will expand the usefulness of the technique and showcase new advances in the field. The primary goal of this work is the determination of fundamental Mössbauer parameters for common rock-forming minerals: the intrinsic isomer shift (δ_I), the characteristic Mössbauer temperature (Θ_M), and the recoil-free fraction (f). The latter parameters are analogous to matrix corrections utilized in electron microscopy, in that they are used to convert peak area ratios determined spectroscopically into valid estimates of actual species concentrations. Although recoil-free fraction, in particular, is key to accurate determinations of $Fe^{3+}/\Sigma Fe$ and Fe site occupancies, fundamental Mössbauer parameters have been characterized for only a handful of minerals due to the difficulty of the measurements.

Minerals in the pyroxene group may well be the most-studied silicates analyzed by Mössbauer spectroscopy. Interpretations based on Mössbauer work on Fe^{2+} distributions in the pyroxene group ($M2M1Si_2O_6$) would greatly benefit from improved knowledge of these Mössbauer fundamental parameters. Pyroxenes are well suited to Mössbauer analysis because there are two possible octahedral sites for Fe^{3+} and Fe^{2+}: the M1 site is a small, regular octahedron, while the M2 site is a larger 6-8 coordinated site (Figure 1). The geometry of the sites varies with composition and space group. The Ca-free orthopyroxenes enstatite ($MgSiO_3$) and ferrosilite ($FeSiO_3$) form a solid solution along the bottom of the quadrilateral and are in the orthorhombic *Pbca* space group. The M2 site in orthopyroxenes is relatively distorted. In the clinopyroxenes, the M2 site is more regular, but its geometry does vary as space group changes. The Ca^{2+}-saturated end-members diopside ($CaMgSi_2O_6$) and hedenbergite ($CaFeSi_2O_6$) belong to the *C2/c* space group, as does the intermediate composition augite (nominally $(Ca,Na)(Mg,Fe,Al,Ti)(Si,Al)_2O_6$). Pigeonite (nominally $(Mg,Fe^{2+},Ca)(Mg,Fe^{2+})Si_2O_6$), which ranges in composition from about Wo_5-Wo_{15}, where Wo is the percentage of Ca-rich pyroxene, $CaSiO_3$, expressed as a fraction of the divalent cations sites. Pigeonite exhibits *C2/c* symmetry at high temperatures (high pigeonite), but on cooling generally transforms to the $P2_1/c$ space group (low pigeonite). Other than between augites and high pigeonites, full solid solution does not exist among the clinopyroxenes because of the differences in structure, and natural pyroxenes are often exsolved or inverted at some scale. Understanding of Fe site occupancy across this range of pyroxene compositions thus requires knowledge of space group and appreciation of the diversity of site geometries across Ca-Mg-Fe composition space.

In pure quadrilateral pyroxenes, Ca^{2+} is the largest cation, so it occupies the M2 site, leaving any remaining space in M2 and all of the M1 site to Fe^{2+} and Mg^{2+}. The latter two

cations are so similar in size (0.78 Å and 0.72 Å, respectively) that they might be predicted to occupy either site. However, Fe^{2+} has a strong octahedral site preference energy (OSPE) resulting from the distortion on the M2 site (Burns 1993), causing Fe^{2+} to favor the M2 site if it is not filled by Ca^{2+}. This preference is not absolute, and the amount of Fe^{2+} partitioned into the M1 and M2 sites depends on the bulk composition of the pyroxene, temperature and pressure of formation, cooling rate, and subsequent metamorphism (e.g. Wang et al. 2005; McCallum et al. 2006). Quantifying the extent of this preference is critical to thermodynamic treatments of pyroxene equilibria, which have been limited by uncertainties related to determination of M1 and M2 occupancies (e.g., Kroll 2003; Zema et al. 2003; Domeneghetti et al. 2005; Alvaro et al. 2011). Because pyroxenes are arguably one of the most common mineral groups occurring on terrestrial planetary surfaces (as well as the Moon), studies of cation ordering in pyroxenes are particularly important because they allow crystallization histories to be better understood.

Many Mössbauer studies of pyroxene (>180 and counting, in peer-reviewed journals, dating back to work on lunar samples) have been published, along with single crystal x-ray diffraction studies that also characterize Mg-Fe ordering in pyroxenes. The vast majority of previous Mössbauer studies have been hampered by the lack of differential recoil-free fraction data that describe how securely the Fe^{2+} and Fe^{3+} are bonded in the M1 and M2 sites in pyroxene. To remedy this situation, this paper examines 658 Mössbauer spectra of 64 synthetic samples covering the pyroxene quadrilateral in roughly 10 mol.% increments, and determines their fundamental Mössbauer parameters as a function of composition. These results will facilitate more accurate determinations of cation site occupancies in pyroxenes. This may in turn help reconcile known discrepancies between Mössbauer and single crystal structure refinements

(as noted by, e.g., Skogby et al. 1992; Domeneghetti and Steffen 1992), and lead to a better understanding of Mg-Fe distribution coefficients and the equilibria they represent.

BACKGROUND

The goal of this study is to characterize the fundamental Mössbauer parameters of synthetic pyroxenes over the Ca-Mg-Fe quadrilateral. The Mössbauer effect arises from the recoilless emission and resonant absorption of nuclear gamma rays in solids. The technique has long been applied to study Fe-bearing industrial and naturally-occurring materials. For this application, the relevant reaction is $^{57}Co_{27} + {}^{0}\beta_{-1} \Rightarrow {}^{57}Fe_{26}$, where the nucleus of the ^{57}Co atom captures an inner electron, transforming a proton to a neutron and creating a nuclear excited state of ^{57}Fe. The excited ^{57}Fe rapidly decays to the stable ^{57}Fe ground state, emitting primarily three γ rays with energies of 136, 122, and 14.4 keV ($t_{1/2}$=97.7x10^{-9} s). If the energy of the 14.4 keV gamma ray is modulated (Doppler-shifted) by placing the ^{57}Co source on an oscillating motor, then a range of gamma-ray energies (±5 x 10^{-7} eV) may be produced, resulting in selective resonant absorption by nuclei of ^{57}Fe atoms in a sample of interest, leading to a Mössbauer spectrum.

However, only a certain fraction of the 14.4 keV emissions and absorptions take place without "recoil", that is, without loss of energy to lattice vibrations. This is the so-called Mössbauer (or recoil-free) fraction, *f*, for which there is no change in the quantum state of the lattice:

$$f = e^{-\frac{4\pi^2 \langle X^2 \rangle}{\lambda^2}}, \qquad (1)$$

where $\langle X^2 \rangle$ is the mean-square vibrational amplitude of the absorbing or emitting nucleus in the solid, and λ is the wavelength of the γ photon. The value of $\langle X^2 \rangle$ varies for different chemical

compounds depending on the site geometry and valence state of the Fe atom. Therefore, *f* depends on the particular crystalline site in which the Fe^{2+} or Fe^{3+} atom is bound, and thus may vary dramatically from mineral group to mineral group. This paper examines subtle variations that occur as a function of changing composition and space group within a single mineral group, the Ca-Mg-Fe pyroxenes. Previous studies (De Grave and Van Alboom 1991, Eeckhout et al. 2000, and Eeckhout and De Grave 2003) have characterized *f* in selected individual pyroxenes within this range (cf. Table 2 in Dyar et al. 2007), but it is difficult to discern trends from these isolated examples.

A typical Mössbauer spectrum of a silicate like the pyroxenes studied here is composed of doublets, each corresponding to Fe in a distinct site or valence state. Each doublet has two parameters that describe the positions of its two peaks: center shift (δ) and quadrupole splitting (Δ). The δ has two contributions: 1) the intrinsic isomer shift (δ_I), arising from the difference in *s*-electron density at the emitting nucleus and that at the absorbing iron nucleus in the sample; and 2) the second-order Doppler shift, δ_{SOD} (i.e., $\delta(T) = \delta_I + \delta_{SOD}(T)$). The δ_{SOD} is the result of the non-zero mean squared velocity of the vibrating ^{57}Fe nucleus, so it has a significant temperature dependence (Eeckhout and De Grave, 2003). Quadrupole splitting arises from an electric field gradient at the nucleus, which produces two hyperfine nuclear energy levels (for non-magnetically ordered materials), and arises when the charge distribution around the nucleus has less than cubic symmetry (as it is in the majority of minerals). These relationships were summarized in an overview paper by Burns and Solberg (1990) in which the center shifts and quadrupole splitting values for many mineral structures were tabulated (see also Dyar et al. 2006). Doublets corresponding to Fe^{2+} and Fe^{3+} can be easily distinguished.

158 In any given spectrum, the areas (*A*) of the doublets can then be computed and used to
159 determine the distribution and abundance (*N*) of Fe^{2+} and Fe^{3+} in the sample. Those peak areas
160 are a function of *N*, peak width Γ, spectral (resonance) saturation *G(x)*, and the recoil-free
161 fraction *f* discussed above. For a spectrum with two doublets (either two Fe sites or two different
162 valences of Fe), Bancroft (1969) used the following general formulation:

163 $$\frac{A_1}{A_2} = C\,\frac{N_1}{N_2}, \text{ where } C = \frac{\Gamma_1 G(X_1) f_1}{\Gamma_2 G(X_2) f_2}. \qquad (2)$$

164 Adapting these equations to Fe^{2+} distribution in synthetic pyroxenes gives:

165 $$\frac{{}^{M1}A^{Fe^{2+}}}{{}^{M2}A^{Fe^{2+}}} = C\,\frac{{}^{M1}N^{Fe^{2+}}}{{}^{M2}N^{Fe^{2+}}}, \text{ where } C = \frac{\Gamma_{M1}}{\Gamma_{M2}}\,\frac{f_{M1}}{f_{M2}}\,\frac{G(X_{M1})}{G(X_{M2})} \quad (3)$$

166 (see also Dyar et al. 2006 for more information).

167 The linewidth (Γ) component is easily addressed by constraining peak widths to vary in
168 pairs, as described above. Saturation (*G(x)*), which may result from a too-thick absorber, may
169 cause underestimation of the Fe content in each site (Skogby et al. 1992), but methods to correct
170 for them as described by Rancourt (1989) are difficult to implement on multiple samples. For
171 pyroxenes, Skogby et al. (1992) proposed a useful empirical correction to zero thickness where:

172 $$\left(\frac{{}^{M1}Fe}{Fe(total)}\right)_{corrected} = \left[\frac{\left(\frac{{}^{M1}Fe}{Fe(total)}\right)_{measured} - 0.004085t}{1 - 0.003031t}\right], \qquad (4)$$

173 and *t* is the thickness calculated using the methods of Long et al. (1983). $^{[M2]}Fe^{2+}$ is then
174 calculated by difference. The third component, which is the effect of differential recoil-free
175 fraction *f*, may be quite significant (De Grave and Van Alboom 1991, Eeckhout and De Grave
176 2003) and thus must be known if truly accurate measurements of site populations are desired

177 from Mössbauer result. Accordingly, the focus of this paper is to determine composition-specific
178 *f* values across the Ca-Mg-Fe pyroxene quadrilateral.

179 Historically, *f* was calculated by measuring the Fe^{3+}/Fe^{2+} in a given mineral species using
180 an independent technique (*e.g.*, wet chemistry), and then calculating a value for *C* based on the
181 first part of equation 3. This method was used by Bancroft and Brown (1975) and by Whipple
182 (1968), who made very careful comparisons between Mössbauer and wet chemical data for a
183 small (15) group of minerals. However, these correction factors apply only to the specific
184 compositions used in those studies, and cannot be used for measurements at temperatures other
185 than 300 K. Only a handful of prior studies have examined the correction factors specifically for
186 pyroxene. By comparing wet chemical results with 295K Mössbauer, Bancroft and Brown
187 (1975) and Whipple (1968) found values of C = 0.89-1.02 for ${}^{M2}f / {}^{M1}f$ for a titanaugite. Skogby
188 et al. (1992) used single crystal x-ray refinements of a ferrosilite and found for ${}^{M2}f / {}^{M1}f$=0.99.

189 Several newer approaches have been used to determine *f* (see Dyar et al. 2006), but the
190 most common was pioneered by Eddy De Grave and Toon Van Alboom (University of Ghent). It
191 is based on Mössbauer spectra acquired over a range of temperatures, usually 20-50 K up to 600-
192 800 K, at 10-50° increments. As part of this calculation, both intrinsic isomer shift (δ_I) and
193 Mössbauer temperature (Θ_M) may be determined from the change in center shift with
194 temperature through the following relation (De Grave et al., 1985):

195 $$\delta(T) = \delta_I - \frac{9}{2}\frac{k_B T}{Mc}\left(\frac{T}{\theta_D}\right)^3 \int_0^{\theta_D/T} \frac{x^3}{e^x - 1} dx \,. \qquad (5)$$

196 Here k_B is the Boltzmann constant, M is the mass of the ^{57}Fe nucleus, c is the speed of light, and
197 T is the absolute temperature. Intrinsic isomer shift (δ_I), which is the center shift that would exist
198 in the absence of (temperature-dependent) lattice vibrations in the absorber (LaFleur and

Goodman 1971), and $\Theta_M \cong \Theta_D$, the Debye temperature of the absorber, under the assumption of a Debye model for its vibrational spectrum. Thus Θ_M and δ_I are fundamental characteristics of Fe cations that are sensitive to both valence state and geometry of the coordination polyhedral surrounding them (see Dyar et al. 2006 and 2008 for more information). The geometry effect is a result of the covalent character of the bond. In minerals like pyroxenes, where site geometry changes with composition and crystal structure, Θ_M and δ_I are expected to vary systematically.

Finally, the recoil-free fraction for each site is calculated using the relation:

$$f(T) = \exp\left[-\frac{3}{2}\frac{E_R}{k_B\theta_D} + \left[1 + 4\left(\frac{T}{\theta_D}\right)^2 \int_0^{\theta_D/T} \frac{x\,dx}{e^x - 1}\right]\right] \quad (6)$$

where E_R is the recoil energy, related to the transition energy, E_γ, by $E_R = E_\gamma^2/2Mc^2$.

This method has been used by several workers to study pyroxenes with a range of compositions. Eeckhout et al. (2000) used the Debye method just discussed to measure *f* in clinopyroxenes over the range from $Mg_{0.91}Fe_{0.09}SiO_3$ to $FeSiO_3$; Eeckhout and De Grave (2003) measured *f* in hedenbergite and diopside; Van Alboom and De Grave (1996) studied riebeckites, and Dyar et al. (2007) characterized orthopyroxenes. A summary of previously-measured *f* values is given in Table 2 of Dyar et al. (2007), but the compositions studied are scattered randomly across pyroxene composition space and all but the latter study utilized natural samples with minor substitutions of other elements. In contrast, the current paper uses synthetic samples to examine changing values of *f* as a systematic function of composition.

METHODS

Sample preparation

Samples for this study were synthesized by Donald Lindsley and colleagues between 1972 and 2006, largely for use as starting materials for equilibria studies. Syntheses used procedures described in Turnock et al. (1973) with minor variations. All samples were prepared from reagent grade chemicals. Specific methods vary by composition, and were chosen to prevent nucleation of pyroxenoids and produce a single, homogeneous pyroxene. Hydrothermal syntheses were controlled to have f_{O2} below FMQ (fayalite-magnetite-quartz) by dissociation of oxalic acid. Samples made in Fe capsules had f_{O2}'s below IW (iron-wüstite) but above IQF (iron-quartz-fayalite). The end result was that no Fe^{3+} was observed in any of these samples.

All samples were cooled to room temperature from 900-1005ºC in 2-10 minutes. Disordering rates quantified for Mg-Fe in orthopyroxenes by Besancon (1981) and Anovitz et al. (1988) suggest that quench times used here were rapid enough to prohibit ordering below the equilibration temperatures. Compositions cover the diopside-hedenbergite-enstatite-ferrosilite quadrilateral in roughly 10 mol% increments (Table 1). Pyroxene compositions and space groups were confirmed by X-ray diffraction.

Pyroxene composition and homogeneity were investigated using the CAMECA SX-100 electron probe microanalyzer (EPMA) at Brown University (see also Klima et al. 2007, 2011). Electron backscatter was used to identify samples with unreacted starting oxides or excess mineral phases. No starting oxides were detected in any samples, though one sample contained trace amounts of fayalite. A number of mid-quadrilateral through high-Ca^{2+} samples contain a small amount of interstitial material that was found to be high in iron and sometimes calcium (Klima et al. 2011). The bulk composition of this phase is indistinguishable from that of a pyroxene, but based on its texture, it is likely to be a quench glass. Minor (generally ≤1%) glass was reported for several of the samples previously described by Turnock et al. (1973). None of

the impurities is more than 1% of the total volume in any given sample; because the detection limit of Mössbauer spectroscopy is roughly 1%, they are unlikely to be a problem in the current study.

The compositions of the pyroxenes as measured by EPMA are presented on a pyroxene quadrilateral in Figure 2 and listed in Table 1. These samples are described and modeled in Klima (2008). The corners of the quadrilateral are the pyroxene end-members diopside (Di), hedenbergite (Hd), Enstatite (En) and Ferrosillite (Fs). Wollastonite ($Ca_2Si_2O_6$, or Wo) would lie at the top of the ternary plot, but compositions with Ca>1 per formula unit (pfu) per Si_2O_6 are not true pyroxenes, but pyroxenoids. Note that a number of the pyroxenes fall within the region of the pyroxene quadrilateral often referred to as the 'forbidden zone' as pyroxenes of that composition are metastable with respect to silica, olivine and augite at ambient atmospheric pressures and temperatures (Lindsley 1983). However, the pyroxenes in that region of the quadrilateral were synthesized at up to 22.5 kbar in order to be well within the pyroxene stability field during the experiments.

Mössbauer spectroscopy

Approximately 10-30 mg of each sample were mixed with sugar under acetone before mounting in a sample holder confined by Kapton® polyimide film tape. Mössbauer spectra were acquired using a source of 100-60 mCi ^{57}Co in Rh on a WEB Research Co. model WT302 spectrometer (Mount Holyoke College). Spectra were acquired from 54 samples at 16 temperatures each ranging from 4-295K. Results were calibrated against a 25 μm α-Fe foil. Spectra were collected in 2048 channels and corrected for nonlinearity via interpolation to a linear velocity scale, which is defined by the spectrum of the 25 μm Fe foil used for calibration.

The WMOSS algorithm fits a straight line to the points defined by the published values of the Fe metal peak positions (as *y* values) and the observed positions in channels (*x* values). Data were then folded before fitting, using the WMOSS Auto-fold procedure that folds the spectrum about the channel value that produces the minimum least squares sum difference between the first half of the spectrum and the reflected second half of the spectrum.

For each sample, the fraction of the baseline due to the Compton scattering of 122 keV gammas by electrons inside the detector was determined by measuring the count rate with and without a 14.4-keV stop filter (~2 mm of Al foil) in the gamma beam. Compton-corrected absorption was calculated for each individual spectrum using the formulation $A/(1 - b)$, where b is the Compton fraction and A is the uncorrected absorption. This correction does not change the results of the fits per se but does allow accurate determination of % absorption in the spectra. It is necessary because the range of energy deposited in the detector by Compton events extends from 0 keV to 40 keV, overlapping both the 14 keV and 2 keV energies deposited by the 14.4 keV gammas. Run times were 6-24 hours per spectrum, and baseline counts ranged from ~2.2 to 14.0 million after the Compton correction.

Spectra were fit with two or three Lorentzian doublets using the MEX_FielDD program acquired from the University of Ghent courtesy of E. DeGrave. Center shifts (CS, or δ), and quadrupole splittings (QS, or Δ) of the doublets were allowed to vary, and widths (full width at half maximum) of all four peaks were coupled to vary in pairs. Errors on center shift and quadrupole splitting of well-resolved peaks are usually ±0.02 mm/s in natural samples (e.g., Skogby et al. 1992), though these can be reduced by use of consistent sample preparation, run conditions, and fitting procedures to ±0.005 mm/s. Reproducibility (precision) of peak areas based on repeated fits using different constraints (δ, Δ, width, and areas constrained in all

possible combinations of individual peaks and pairs) and fitting models (Lorentzian, Gaussian, quadrupole splitting distributions) are ±0.3% absolute for these well-resolved spectra; accuracy has been determined in previous analogous studies of amphiboles to be ±3-5% (Dyar, 1989). For absolute site occupancy measurements based on peak areas, saturation corrections are usually considered. Skogby et al. (1992) have described the appropriate empirical correction to zero thickness and Dyar et al. (2007a) applied it to a subset of the samples studied here to assess its magnitude; peak areas changed very little (<1% of the total area). Moreover, *f* is determined from center shift variations, not peak areas. Thus thickness corrections were not applied in this current study because they were not relevant to the determination of fundamental Mössbauer parameters.

Finally, the fundamental Mössbauer parameters intrinsic isomer shift (δ_I), Mössbauer temperature (Θ_M), and the recoilless fraction (*f*) were determined for each sample using the temperature dependence of the center sift as described above (equations 5 and 6). A sample model is shown in Figure 3.

RESULTS

Representative fits to selected pyroxenes are listed in Table 2 and shown in Figure 4. Results show variations in all the Mössbauer parameters studied: center shift, quadruple splitting, area, recoil-free fraction, Mössbauer temperature, and intrinsic isomer shift. Of course, these parameters are to some extent interrelated. Peak areas should change with composition, and we use the temperature dependence of the center shift to determine the characteristic Mössbauer temperature, and in turn calculate *f*. But it is helpful to first discuss the results of each parameter separately and then to consider how their variations affect fundamental Mössbauer parameters.

312 In most cases, data for extremely low Fe samples (e.g., En_{90}) do not fit observed trends well,
313 likely because spectra for such low Fe samples are of low statistical quality. Thus the following
314 summation focuses largely on samples with >0.4 cations of Fe pfu.

315 **Center shift**

316 For the M1 site at all temperatures, Figure 5 shows that there is a slight but systematic
317 increase of ~0.02 mm/s in center shift along the En-Fs join from Fs_{20} to Fs_{100} (δ = 1.167-1.186
318 mm/s at 295K). Generally increases in center shift are associated with decreasing *s*-electron
319 density around the nucleus, so this change must reflect variation in the type and (more likely)
320 lengths of bonds with oxygens coordinated to the Fe atoms. As the slightly larger Fe^{2+} cation
321 (ionic radius = 0.78 Å; Dyar and Gunter 2008) substitutes for Mg^{2+} (0.72 Å), it ought to increase
322 the size of the sites and thus distribute the *s*-electrons over a larger area (decreasing their overall
323 density). This observation is consistent with the variation seen across the orthopyroxene series
324 for the M1 site, and supported by the work of Turnock et al. (1973), who observed that unit cell
325 parameters of orthopyroxenes increase from enstatite to ferrosilite. However, for the M2 site, δ
326 decreases along the En-Fs join (ca. 1.150-1.132 mm/s for 295K) as Fe is added across the
327 orthopyroxenes – the opposite of the trend for M1. Perhaps this is reflecting a change in the
328 covalent character of bonds surrounding the Fe atom, which may result in distortion. The size of
329 M1 alone may be responsible for the change in the overall unit cell size.

330 As the space group and mineral species change with the addition of Ca to these
331 pyroxenes, systematic variations of δ with composition are not so clearly apparent. The δ_{M1}
332 values for Fe-rich compositions are generally higher than those for Mg-rich compositions,
333 especially in low-Ca and high-Ca samples; the reverse is true for δ_{M2}. Other possible trends are
334 unclear, likely because of changes to the structures from one pyroxene polytype to another.

335 **Quadrupole splitting**

336 Quadrupole splitting (Δ) is sensitive to oxidation state and site geometry. In these
337 pyroxenes, Fe^{2+} ($3d^6$), is in a high spin $t_{2g}^4 e_g^2$electronic configuration. The sixth electron
338 populates the three degenerate (all the same energy) t_{2g}^4 levels equally, but distortion of the
339 octahedral environment, as occurs through Jahn-Teller distortion, lifts the degeneracy of the t_{2g}^4
340 levels, leading to unequal occupancy of the *d* orbitals and a larger contribution to Δ from the
341 electronic field. The resultant asymmetry in the lattice field causes Fe^{2+} to split the $I = 3/2$ level,
342 so the larger the Δ, the more distorted the coordination polyhedron surrounding the Fe atom.

343 Some variation in Δ is evident across the pyroxene Ca-Mg-Fe quad studied here (Figure
344 6). For the orthopyroxenes, Δ_{M1} increases slightly from enstatite (Δ = 2.467 mm/s at 295K) to
345 ferrosilite (Δ = 2.534mm/s), while Δ_{M2} *de*creases (e.g., at 80K, $\Delta_{enstatite} \approx 2.108$ mm/s and
346 $\Delta_{ferrosilite} = 1.985$ mm/s). This implies that adding Fe^{2+} to the M1 site changes the covalent
347 character of bonds surrounding the Fe atom, increasing M1 distortion, while replacing Mg in the
348 M2 site makes that site more regular in shape. Crystal structure refinement data are insufficient
349 to demonstrate this trend because the samples studied do not have the same cooling histories as
350 those here.

351 As Ca is added to what becomes the clinopyroxene structure, the larger Ca cation causes
352 the M2 site to become bigger and more regular but causing the local environment around Fe
353 cations to become more distorted. This is reflected in Δ, which increases slightly for both M1 and
354 M2 until near the diopside/hedenbergite solid solution, where the trends become obscured by the
355 splitting of the M2 site into two distributions. Along the diopside-hedenbergite continuum,
356 values of Δ are low for M1 and unusually high for M2 at all temperatures (Figure 6).

357 **Area**

For orthopyroxenes, because the area of the paired peaks in each doublet is proportional to the abundance of Fe in that site, Fe^{2+} should be evenly distributed between M1 and M2 at the highest Fe contents (Fs_{100}), which is true within the accuracy stated above (Figure 7), even before correction for *f*. As Mg is added along the orthopyroxene join, Fe ordering into M2 is immediately apparent, with the M1 doublet rapidly decreasing in intensity relative to M2 as Mg is added, presumably first to the M1 sites. As a result, the spectra of the highest Mg samples are dominated by the M2 doublet, though there is always small shoulder representing Fe^{2+} in M1 (see also Dyar et al. 2007). These results support the preference of Fe^{2+} for the M2 site, presumably due to the strong octahedral site preference energy (OSPE) for Fe^{2+} in the more distorted site. Temperature can also play a role in determining the extent of this preference. Because all our samples were prepared in exactly the same way, variations due to cooling rate can be ruled out. However, it must be noted that the site occupancies determined here are neither universal nor specific to their compositions, but will vary with cooling rate (e.g., Ganguly 1982; Brizi et al. 2001; Domenghetti et al. 2005).

At intermediate compositions within the quadrilateral, the addition of Ca and the transition to the clinopyroxene structure also changes the ordering of Fe as reflected in the M1 and M2 areas. Along the diopside-hedenbergite join, 100% of the Fe must be in the M1 site because the M2 site is fully occupied by Ca, and this is what is observed. Below that join, Fe^{2+} continues to display a strong preference for M2. For example, there is no Fe^{2+} in M2 in a $Wo_{50}Fs_{50}$ pyroxene, but at only slightly lower Ca contents, $Wo_{40}Fs_{60}$, 67% of the Fe is in M2.

Recoil-free fraction

Recoil-free fraction is the most important parameter for practical applications of Mössbauer spectroscopy that depend on accurate site occupancies, and the results shown in

Figure 8 provide a useful source for estimation of *f* for many common pyroxenes. Systematics are difficult to discern because of the changing space group and crystal structure across the quad. However, for the M1 site at all temperatures, there is a slight but systematic decrease in recoil-free fraction from Fs_{10} to Fs_{100}. In general, Mg-rich compositions have slightly higher *f* values than Fe-rich samples with the same Ca content. Value of *f* close to the diopside-hedenbergite join are the lowest of those in the entire quadrilateral. For the M2 site, there is also a small but consistent decrease in recoil-free fraction from Fs_{10} to Fs_{100}. As Ca is added and the structure changes from orthopyroxene to clinopyroxene, *f* values increase. At high Ca contents when the M2 doublet splits into two, the M2a doublet has very low *f* values and the M2b has the highest *f* values of the entire quadrilateral.

Intrinsic isomer shift and Mössbauer temperature

The fundamental Mössbauer parameters δ_I and Θ_M show trends across composition space (Figure 9). The value of δ_I is generally higher for the M1 (ignoring En_{90}, which is a poor-quality spectrum) site than for M2. In the orthopyroxenes, δ_I increases slightly from En to Fs for M1, with an opposite trend for M2. The Θ_M values are lower for M2 than for M1, and decrease from Mg-rich to Fe-rich for both M1 and M2. These are generally analogous trends to those observed for center shift. Because the Fe valence state does not change, these variations must reflect changes in geometry of Fe coordination polyhedra, which are a function of the covalency of the bonds and the occupancies of the surrounding sites.

Values for δ_I and Θ_M show similar trends to those determined for several pyroxenes by De Grave and Van Alboom (1991). As stated earlier, δ_I is a characteristic of a given site

The Θ_M values are in the range from 300-500K, consistently lower than those for Fe^{3+} in silicates and oxides. Although Θ_M may not have a direct physical significance, as noted by De

Grave and Van Alboom (1991), and Herber (1984), it is a measure of the strength of the bond between the Fe atoms and the lattice, such that a higher Mössbauer temperature reflects a stronger bond with the lattice. It may also be useful in comparing sites between different mineral groups, and thus is reported here. However, care must be taken in comparing values of Θ_M with Θ_D values determined by other methods.

Multiple M2 doublets

The high Ca diopside/hedenbergite samples studied here are all better fit by models with two M2 doublets rather than a single distribution. This phenomenon has been reported previously for naturally-occurring pyroxenes by Dowty and Lindsley (1973) and Seifert (1983) and observed by many subsequent workers (e.g., Dyar et al. 1989). Seifert (1983) suggests that when trivalent cations such as Fe^{3+} and Al^{3+} substitute into M1 sites, distortion occurs. He proposed that there are two types of M2 sites: Fe^{2+} in M2 surrounded by only divalent cations in M1 (such as Mg), and Fe^{2+} in M2 surrounded by M1 sites containing at least one trivalent substitution. Because the samples in this current study are all completely reduced and have no Al, an alternative explanation is needed. All the samples requiring two M2 doublets are high in Ca, so one cause of the two distributions might be site distortion caused by the introduction of Ca into the structure. Alternatively, it is possible that these high-Ca pyroxenes are exsolved at scales finer than are visible by the electron microprobe, and that these samples actually consist of two different coexisting pyroxenes with slightly different M2 site geometries.

DISCUSSION

The most significant results of this study are the values of recoil-free fraction generated across the compositional range. Recoil-free fraction is a measure of the rigidity or strength of the

bonds surrounding the Fe atom (Dyar et al. 2006). If so, then the trends observed in changes in the Mössbauer parameters with composition ought to reflect changes in the crystal structure itself. Thus, observed variations in recoil-free fraction are related to factors that also contribute to center shift, namely the Coulombic interactions between the nuclear and electronic charge distributions at every Fe site. Center shift is strictly a function of the *s*-electronic charge density at the nucleus, although this density is also affected by shielding from *p*, *d*, and *f* electrons and by participation of electrons in bonding.

Given these relationships and dependencies, it should be expected that recoil-free fractions should be related to the geometries of the M1 and M2 coordination polyhedra in pyroxene that also change with composition. Fortunately, the latter are well-characterized. Single crystal structure refinements (SREF) of pyroxenes containing the cations Si, Mg, Ca, and Fe were collected from the American Mineralogist Crystal Structure Database using data from natural and synthetic Ca-Mg-Fe pyroxenes from Freed and Peacor (1967), Clark and Papike (1968), Morimoto and Guven (1970), Burnham et al. (1971), Clark et al. (1971), Cameron et al. (1973), Smyth (1973), Ohashi et al. (1975), Sueno et al. (1976), Angel et al. (1989), Molin (1989), Raudsepp et al. (1990), Hazen et al. (1993), Hugh-Jones and Angel (1994), Hugh-Jones et al. (1994), Yang and Ghose (1995), Harlow (1996), Zhang et al. (1997), Heuer et al. (2005), and Nestola et al. (2008). Using those crystal structure data and the CrystalMaker software package, several parameters describing the M1 and M2 sites were calculated. These included:

- O3-O3-O3 bond angles (Figure 11)
- O3-O3 distance along edge between two adjacent M2 sites
- O3-M2-O3 bond angles
- O1-M1-O1 bond angles

- O1-M2-O1 bond angles
- O2-M1-O2 bond angles
- O1-O1 distances along edges between M1 sites
- O1-O1 distances along edges between M1 and M2 sites
- mean bond length for M1 and M2 sites
- mean octahedral quadratic elongation (λ) for M1 and M2
- angular variance (σ_{M1} or σ_{M2})

The latter two parameters were devised by Robinson et al. (1971) to summarize variations in bond length and bond angle. Angular variance (σ) is calculated using the expression:

$$\sigma = \sum_{i=1}^{n}\left(\theta_i - \theta_{avg.}\right)^2/(n-1), \qquad (7)$$

where θ_i is the measured angle in the crystal structure (there are n=12 angles in a 6-coordinated site) and θ_{avg} is the bond angle for a perfect octahedron (all angles are 90º). The quadratic elongation parameter (λ) provides a quantitative measurement of polyhedral distortion that is independent of polyhedral size:

$$\lambda = \sum_{i=1}^{n}\left(\frac{l_i}{l_0}\right)^2/n, \qquad (8)$$

where l_i is the measured bond distance (where n = 6 for 6-coordination) and l_0 is the bond distance in a perfect (undistorted, equal volume) octahedron.

Each of these parameters was plotted on a scatter diagram against Ca, Mg, and Fe contents to assess which characteristics of the crystal structure depend most heavily on composition in this range. Most yielded random distributions, but some interesting trends were evident. Mean M1 bond length generally decreases with increasing Mg/decreasing Fe while

472 being unaffected by Ca (Figure 10). Mean M2 bond length increases with increasing Ca (Figure
473 10) but shows no systematic trends as a function of Fe or Mg variation. Cameron and Papike
474 (1980) show near-linear relationship between the mean M-O distance and the mean ionic radius
475 of the cations in the M1 and M2 sites. The mean distance between the cation and the surrounding
476 oxygens varies most as a function of Ca (ionic radius = 1.0 Å) content, particularly in the M2 site
477 that is occupied by Ca. Substitution of Mg (ionic radius = 0.72 Å) for Fe (0.78 Å) affects the M1
478 site more because that site contains (in these samples) solely Fe and Mg with no Ca.

479 The calculations also show that the O3-M2-O3 angle decreases with increasing Fe
480 content but increases with increasing Ca. The O1-M2-O1 angle decreases with increasing Ca
481 content. Increasing Ca causes the O1-M1-O1 bond angles to increase. The combined effects of
482 changing bond lengths and bond angles causes mean octahedral quadratic elongation (Figure 12)
483 and angular variance (not shown) both to decrease with increasing Ca. Both sites become more
484 regular and less distorted as Ca is added.

485 These trends can be compared with analogous plots of recoil-free fraction for
486 compositions where both SREF and Mössbauer data were available (Figure 13). A limitation of
487 this comparison is the fact that in most cases, the two types of measurements were not made on
488 the identical samples, and thus variations in cooling history may have led to cation site
489 occupancy differences. However, the aggregate results show some trends.

490 Consider first the possible relationship between bond length and recoil-free fraction.
491 Although Ca, Fe, and Mg have the same charge, the bond lengths vary because substitution of
492 the larger Ca^{2+} cation in the M2 site increases the size of the coordination polyhedra around the
493 M2 site. Thus the strength of the bond between the cations and the neighboring oxygen anions is
494 reduced. The electrostatic bond strength of an ionic bond is defined as the charge on the cation

495 divided by its coordination number, which is a proxy for bond length. Thus the longer the bonds
496 between the M cations and the surrounding O anions, the weaker the bond strength.

497 It was noted earlier that the mean M1 cation to oxygen distance decreases as Mg (the
498 smallest of these three cations) is added. Figure 13 shows that increasing Mg generally causes
499 recoil-free fraction to increase. So smaller bond lengths cause higher *f* values for M1. This
500 comparison is less compelling for the M2 site, where there are no apparent systematic
501 relationships between bond length and cation substitutions.

502 However, *f* is also related to mean octahedral quadratic elongation, as seen through
503 comparison of Figures 12 and 13. For M1, the trend is toward less distortion with increasing Ca.
504 As Ca is added to the structure and Mg is removed, the *f* values for M1 decrease as the site
505 becomes more regular. There are no clear-cut systematics for changes in *f* as a function of
506 composition for the M2 site.

507 These conclusions are important because bond strength and distortion are likely related to
508 the "rigidity" of the coordination polyhedra, which is then reflected in the magnitude of *f*. As
509 more total Mg substitutes into M1 or M2, the M1 site becomes more distorted as the M1 cation
510 to oxygen bonds shorten. Higher Mg and the smaller sites thus result in higher values of *f*,
511 suggesting that the smaller overall sites hold the Fe^{2+} cations more firmly and affect the fraction
512 of recoil-less emission events. As Ca is added to pyroxene, increasing overall M2 bond lengths
513 and making the site less distorted, the resultant longer (and thus weaker bonds) should result in
514 lower values of *f*. It would be useful to have single crystal structure refinement data for the
515 identical samples for which we have Mössbauer data; those studies are already in progress.

516 Some of the information lost in the *x*-*y* plots shown in Figures 12 and 13 is reclaimed by
517 re-inspection of the quadrilaterals (e.g. Figure 8). For orthopyroxenes from enstatite to ferrosilite,

518 the change from smaller, distorted sites to larger, more regular M1 sites, causes a decrease in *f*
519 for both M1 and M2. From enstatite to diopside, there is generally a decrease in *f*. From
520 ferrosilite to hedenbergite, the site size also increases, but there are no clear-cut changes in *f*.
521 Taken together, these results do suggest that larger sites with lower bond strengths and more
522 regular coordination polyhedra result in lower values of *f*; i.e., that the Fe^{2+} cation is held less
523 rigidly (less tightly bound) in the crystal structure and thus recoils more strongly. This result is in
524 keeping with theoretical expectations, but until this study was never demonstrated for minerals
525 with experimental data.
526

527 ## ACKNOWLEDGMENTS

528 We are extremely grateful to Don Lindsley and Allan Turnock for providing us with the
529 pyroxenes for this study along with frequent good advice. We are very grateful to David Agresti
530 and two anonymous reviewers whose comments greatly improved this paper. This work was
531 supported by NSF grant EAR-0439161and NASA grants NNX07AP41G, NNX10AH62G
532 (LASER), and NNX11AO95G (PGG). Student support also came from the Massachusetts Space
533 Grant Consortium.
534

535 ## REFERENCES CITED

536 Alvaro, M., Camara, F., Donemghetti, M.C., Nestola, F., and Tazzoli, V. (2011) HT $P2_1/c$-C_2/c
537 phase transition and kinetics of Fe^{2+}-Mg disorder of an Fe-poor pigeonite: implications
538 for the cooling history of ureilites. Contributions to Mineralogy and Petrology, 162, 599-
539 613.

Angel, R.J., Gasparik, T., and Finger, L.W. (1989) Crystal structure of a Cr^{2+}-bearing pyroxene. American Mineralogist, 74, 599-603.

Anovitz, L.M., Essene, E.J., and Dunham, E.J. (1988) Order-disorder experiments on orthopyroxenes: implications for the orthopyroxene geospeedometer. American Mineralogist, 73, 1060.1073.

Bancroft, G.M. (1969) Quantitative site populations in silicate minerals by the Mössbauer effect. Chemical Geology, 5, 255-258.

Bancroft, G.M., and Brown, J.R. (1975) A Mössbauer study of coexisting hornblendes and biotites: Quantitative Fe^{3+}/Fe^{2+} ratios. American Mineralogist, 60, 265-272.

Bertolo, S., Nimis, P., and Dal Negro, A. (1994) Low-Ca augite from experimental alkali basalt at 18 kbar: Structural variation near the miscibility gap Atomic parameters from ICSD. American Mineralogist, 79, 668-674.

Besancon, J.R. (1981) Rate of cation disordering in orthopyroxenes. American Mineralogist, 66, 965-973.

Brizi, E., Molin, G.M., Zanazzi, P.F., and Merli, M. (2001) Ordering kinetics of Mg–Fe^{2+} exchange in a $Wo_{43}En_{46}Fs_{11}$ augite. American Mineralogist, 86, 271–278.

Brown, G. E., Prewitt, C. T., Papike, J. J., and Sueno, S. (1972) A comparison of the structures of low and high pigeonite. Journal of Geophysical Research. 77, 5778-5789.

Burnham, C.W., Ohashi, Y., Hafner, S.S. and Virgo, D. (1971) Cation distribution and atomic thermal vibrations in an iron-rich orthopyroxene. American Mineralogist, 56, 850-876.

Burns R.G. (1993) Mineralogical Applications of Crystal Field Theory, 2nd edition. Cambridge University Press, Cambridge.

Burns R.G., and Solberg T.C. (1990) Spectroscopic characterization of minerals and their

surfaces. ACS Symposium Series, 415, 262-283.

Cameron, M., and Papike, J.J. (1980) Crystal chemistry of silicate pyroxenes. Mineralogical Society of America Reviews of Mineralogy, 7, 5-92.

Cameron, M., Sueno, S., Prewitt, C.T., and Papike, J.J. (1973) High-temperature crystal chemistry of acmite, diopside, hedenbergite, jadeite, spodumene, and ureyite. American Mineralogist, 58, 594-618.

Clark, J.R. and Papike, J.J. (1968) Crystal-chemical characterization of omphacites American Mineralogist, 53, 840-868.

Clark, J.R., Ross, M., and Appleman, D.E. (1971) Crystal chemistry of a lunar pigeonite. American Mineralogist, 56, 888-908.

De Grave E., Verbeeck A.E., and Chambaere D.G. (1985) Influence of small aluminum substitutions on the hematite lattice. Physics Letters, 107A, 181-184.

De Grave, E. and Van Alboom, A. (1991) Evaluation of ferrous and ferric Mössbauer fractions. Physics and Chemistry of Minerals, 18, 337-342.

Domeneghetti, M.C., Zema M, and Tazzoli V (2005) Kinetics of Fe^{2+}–Mg order-disorder in *P*21/*c* pigeonite. American Mineralogist, 90, 1816–1823.

Domeneghetti, M.C., and Steffen, G. (1992) M1, M2 site populations and distortion parameters in synthetic Mg-Fe orthopyroxenes from Mössbauer spectra and X-ray structure refinements. Physics and Chemistry of Minerals, 19, 298-306.

Dowty, E., and Lindsley, D.H. (1973) Mössbauer spectra of synthetic hedenbergite-ferrosilite pyroxenes. American Mineralogist, 58, 850-868.

584 Dyar M.D., Agresti D.G., Schaefer M., Grant C.A., and Sklute E.C. (2006) Mössbauer
585 spectroscopy of earth and planetary materials. Annual Reviews of Earth and Planetary
586 Science, 34, 83-125.
587 Dyar, M.D., Klima, R.L., and Pieters, C.M. (2007) Effects of differential recoil-free fraction on
588 ordering and site occupancies in Mössbauer spectroscopy of orthopyroxenes. American
589 Mineralogist, 92, 424-428.
590 Dyar, M.D., and Gunter, M.C. (2008) Mineralogy and Optical Mineralogy: A Three-
591 Dimensional Approach. Textbook. Mineralogical Society of America.
592 Dyar, M.D., Schaefer, M.W., Sklute, E.C., and Bishop, J.L. (2007) Mössbauer spectroscopy of
593 phyllosilicates: effects of fitting models on recoil-free fraactions and redox ratios. Clay
594 Minerals, 43, 1-31.
595 Dyar, M.D., McGuire, A.V., and Ziegler, R.D. (1989) Redox equilibria and crystal chemistry of
596 coexisting minerals from spinel lherzolite mantle minerals. American Mineralogist, 74,
597 969-980.
598 Dyar, M.D., Schaefer, M.W., Sklute, E.C., and Bishop, J.L. (2008) Mössbauer spectroscopy of
599 phyllosilicates: Effects of fitting models on recoil-free fractions and redox ratios. Clay
600 Minerals, 43, 3-33.
601 Eeckhout, S.G. and De Grave, E. (2003a) Evaluation of ferrous and ferric Mössbauer fractions.
602 Part II. Physics and Chemistry of Minerals, 30, 142-146.
603 Eeckhout, S.G., and De Grave, E. (2003b) ^{57}Fe Mössbauer studies of Ca-rich, Fe-bearing
604 clinopyroxenes: Part I. Paramagnetic spectra of magnesian hedenbergite. American
605 Mineralogist, 88, 1129-1137.

606 Eeckhout, S.G., De Grave, E., McCammon, C.A., and Vochten, R. (2000) Temperature
607 dependence of the hyperfine parameters of synthetic $P2_1/c$ Mg-Fe clinopyroxenes along
608 the $MgSiO_3$-$FeSiO_3$ join. American Mineralogist, 85, 943-952.
609 Freed, R.L., and Peacor, D.R. (1967) Refinement of the crystal structure of johannsenite.
610 American Mineralogist, 52, 709-720.
611 Ganguly J (1982) Mg–Fe order-disorder in ferromagnesian silicates II. In: Saxena SK (ed)
612 thermodynamics: kinetics and geological applications advances in physical geochemistry,
613 vol 2. Springer, Berlin, pp. 58–99.
614 Harlow, G.E. (1996) Structure refinement of a natural K-rich diopside: The effect of K on the
615 average structure. American Mineralogist, 81, 632-638.
616 Hazen, R.M., Finger, L.W., and Ko, J. (1993) Effects of pressure on Mg-Fe ordering in
617 orthopyroxenes synthesized at 11.3 GPa and 1600º C. American Mineralogist, 78, 1336-
618 1339.
619 Herber, R.H. (1984) Structure, bonding, and the Mössbauer lattice temperature. In: Herber, R.H.
620 (ed) Chemical Mössbauer spectroscopy. Plenus Press, New York, pp. 199-216.
621 Heuer, M., Huber, A.L., Bromiley, G.D., Fehr, K.T., and Bente, K. (2005) Characterization of
622 synthetic hedenbergite ($CaFeSi_2O_6$)-petedunnite ($CaZnSi_2O_6$)solid solution series by X-
623 ray single crystal diffraction. Physics and Chemistry of Minerals, 32, 552-563.
624 Hugh-Jones, D. A., and Angel, R. J. (1994) A compressional study of $MgSiO_3$ orthoenstatite up
625 to 8.5 Gpa Sample: P = 0 Gpa. American Mineralogist, 79, 405-410.
626 Hugh-Jones, D.A., Woodland, A.B., and Angel, R.J. (1994) The structure of high-pressure C2/c
627 ferrosilite and crystal chemistry of high-pressure C2/c pyroxenes. American Mineralogist,
628 79, 1032-1041.

Klima, R.L., Dyar, M.D., and Pieters, C.M. (2007), Spectroscopy of synthetic Mg-Fe Pyroxenes I: Spin-allowed and spin-forbidden crystal field bands in the visible and near-infrared, Meteoritics and Planetary Science, 42, 235-253.

Klima, R.L. (2008) Integrated spectroscopy of Mg-Fe-Ca pyroxenes: A foundation for modern compositional analysis of planetary surfaces. Ph.D. thesis, Brown University, Providence, Rhode Island, USA.

Klima, R.L., Dyar, M.D., and Pieters, C.M. (2011) Near-infrared spectra of clinopyroxenes: Effects of calcium content and crystal structure. Meteoritics and Planetary Science, 46, 379-395.

Kroll, H. (2003) Rate equations for non-convergent order-disorder processes – a review and application to orthopyroxene. European Journal of Mineralogy, 15, 7-19.

Lafleur, L.D. and Goodman, C. (1971) Characteristic temperatures of the Mössbauer fraction and thermal-shift measurements in iron and iron salts. Physics Reviews B, 4, 2915-2920.

Lindsley, D.A. (1983) Pyroxene thermometry. American Mineralogist, 68, 477-93.

Long, G.J., Cranshaw, T.E., and Longworth, G. (1983) The ideal Mössbauer effect absorber thicknesses. Mössbauer Effect Reference Data Journal, 6, 42-49.

McCallum, I.S., Domeneghetti, M.C., Schwartz, J.M., Mullen, E.M., Zeman, M., Camara, F., McCammon, C., and Ganguly, J. (2006) Cooling history of lunar Mg-suite gabbronorite 76255, troctolite 76535 and Stillwater pyroxenite SC-936: The record in exsolution and ordering in pyroxenes. Geochimica et Cosmochimica Acta, 70, 6068-6078.

McCammon, C.A. (1994) A Mo□ssbauer milliprobe: Practical considerations. Hyperfine Interactions, 92, 1235–1239.

Molin, G.M. (1989) Crystal-chemical study of cation disordering in Al-rich and Al-poor orthopyroxenes from spinel lherzolite xenoliths. American Mineralogist, 74, 593-598.

Morimoto, N. and Guven, N. (1970) Refinement of the crystal structure of pigeonite. American Mineralogist, 55, 1195-1209.

Nestola, F., Ballaran, T.B., Balic-Zunic, T., Secco, L., and Dal Negro, A. (2008) The high-pressure behavior of an Al- and Fe-rich natural orthopyroxene sample. American Mineralogist, 93, 644-652.

Ohashi, Y., Burnham, C. W., Finger, L. W. (1975) The effect of Ca-Fe substitution on the clinopyroxene crystal structure $Fs_{80}Wo_{20}$. American Mineralogist, 60,423-434.

Rancourt, D.G. (1989) Accurate site populations from Mössbauer spectroscopy. Nuclear Instruments and Methods in Physics Research, B44, 199-210.

Raudsepp, M., Hawthorne, F.C., and Turnock, A.C. (1990) Crystal chemistry of synthetic pyroxene on the join $CaNiSi_2O_6$-$CaMgSi_2O_6$ (diopside): A Reitveld refinement study. American Mineralogist, 75, 1274-1281.

Robinson, K., Gibbs, G.V., and Ribbe, P.H. (1971) Quadratic elongation: A quantitative measure of distortion in coordination polyhedral. Science, 172, 567-570.

Seifert, F . (1983) Mössbauer line broadening in aluminous orthopyroxenes: Evidence for next nearest neighbors interactions and short-range order. Neues Jahrbuch für Mineralogie Abhandlungen, 148, 141-162.

Skogby H., Annersten H., Domeneghetti M.C., Molin G.M., and Tazzoli V. (1992) Iron distribution in orthopyroxene: A comparison of Mössbauer spectroscopy and X-ray refinement results. European Journal of Mineralogy, 4, 441-452.

673 Smyth, J.R. (1973) An orthopyroxene structure up to 850ºC. American Mineralogist, 58, 636-
674 648.
675 Sueno, S., Cameron, M., Prewitt, C.T. (1976) Orthoferrosilite: High-temperature crystal
676 chemistry T = 24 deg C. American Mineralogist, 61, 38-53.
677 Turnock, A.C., Lindsley, D.H., and Grover, J.E. (1973) Synthesis and unit-cell parameters of Ca-
678 Mg-Fe pyroxenes. American Mineralogist, 58, 50-59.
679 Van Alboom, A., and De Grave, E. (1996) Temperature dependence of the 57Fe Mössbauer
680 parameters in riebeckite. Physics and Chemistry of Minerals, 23, 377-386.
681 Wang, L.P., Moon, N., Zhang, Y.X., Dunham, W.R., and Essene, E.J. (2005) Fe-Mg disorder in
682 clinopyroxenes. Geochimica et Cosmochimica Acta, 69, 5777-5788.
683 Whipple, E.R. (1968) Quantitative Mössbauer spectra and chemistry of iron. Earth and
684 Atmospheric Science, 187 pp. Massachusetts Institute of Technology, Cambridge.
685 Yang, H. and Ghose, S. (1995) A transitional structural state and anomalous Fe-Mg order-
686 disorder in Mg-rich orthopyroxene, $(Mg_{0.75}Fe_{0.25})_2Si_2O_6$. American Mineralogist, 80, 9-20.
687 Zema, M., Tarantino, S.C., Domeneghetti, M.C., and Tazzoli, V. (2003) Ca in orthopyroxene:
688 structural variations and kinetics of the disordering process. European Journal of
689 Mineralogy, 15, 373-380.
690 Zhang, L., Ahsbahs, H., Hafner,S.S., and Kutoglu, A. (1997) Single-crystal compression and
691 crystal structure of clinopyroxene up to 10Gpa. American Mineralogist, 82,245-258.

Table 1. Sample Compositions

Sample	As Synthesized			EMPA		
Name	Wo	En	Fs	Wo	En	Fs
px002	0	80	20	0	80	20
px003	0	75	25	0	77	23
px004	0	50	50	0	50	50
px005	0	40	60	0	43	57
px006	0	25	75	0	25	74
px009	10	45	45	10	43	47
px010	10	63	27	7	73	20
px011	10	36	54	14	36	50
px012	5	48	48	3	62	35
px013	8	46	46	14	56	31
px015	5	67	29	2	79	19
px017	20	64	16	23	65	12
px018	10	72	18	8	78	14
px019	20	56	24	16	69	15
px020	0	17	83	0	18	82
px021	0	8	92	0	9	91
px022	0	75	25	0	75	25
px023	0	30	70	0	30	70
px024	0	17	83	0	18	82
px025	0	35	65	0	35	65
px026	0	70	30	0	72	28
px027	0	80	20	0	80	20
px028	0	25	75	0	25	75
px029	0	15	85	0	14	86
px030	0	70	30	0	72	28
px031	0	50	50			
px033	50	40	10	49	42	8
px034	0	50	50			
px036	50	20	30	49	27	24
px037	50	15	35	49	16	35
px039	50	25	25	49	29	22
px041	50	0	50	49	0	51
px043	50	40	10	49	45	6
px044	50	35	15	49	43	8
px048	10	14	77			
px049	10	14	77	19	11	70
px050	15	21	64	23	19	58
px051	20	40	40	27	39	34
px053	10	23	68	8	23	70
px054	15	7	78	23	6	70
px055	20	20	60	26	18	56
px056	20	20	60	22	18	60
px057	20	32	48	25	36	39
px058	25	30	45	27	28	45
px061	0	0	100	0	0	100
px064	0	98	3	0	97	3
px065	0	90	10	0	90	10
px066	30	18	53	38	15	48
px067	30	49	21	39	52	9
px068	30	28	42	38	29	33
px070	40	15	45	45	14	41
px071	40	24	36	46	23	31
px073	30	35	35	39	36	25
px074	30	21	49	39	24	37
px075	40	48	12	45	46	9
px076	40	10	50	46	18	35
px077	40	55	5	45	52	3
px079	40	30	30	47	38	15
px082	50	0	50	49	1	50
px083	50	0	50	51	0	49
px085	30	0	70	39	0	61
px087	20	0	80	29	0	71
px088	10	0	90			
px001	0	100	0	0	100	0

Wo = % wollastonite, $CaSiO_3$, En = %enstatite, $MgSiO_3$, Fs = %ferrosilite, $FeSiO_3$. EMPA refers to the known composition from electron probe microanalyses.

Table 2. Sample Data for 8 Selected Samples

T (K)		px024	px015	px053	px013	px066	px075	px079	px082
	Wo	0	2	8	14	38	45	47	49
	En	18	79	23	56	15	46	38	1
	Fs	82	19	70	31	48	9	15	50
	M1 Θ_M (K)	376	393	409	396	356	363	367	361
	M1 δ_I (mm/s)	1.41	1.41	1.42	1.41	1.41	1.41	1.40	1.42
	M2a Θ_M (K)	329	362	345	339	372	331	379	
	M2a δ_I (mm/s)	1.37	1.38	1.36	1.37	1.41	1.40	1.41	
	M2b Θ_M (K)					437	445	500	
	M2b δ_I (mm/s)					1.35	1.38	1.38	
295	M1 δ (mm/s)	1.18	1.19	1.19	1.18	1.18	1.18	1.17	1.19
	M1 Δ (mm/s)	2.51	2.59	2.49	2.54	2.66	2.63	2.66	2.26
	M1 Width (mm/s)	0.29	0.30	0.37	0.35	0.29	0.30	0.31	0.34
	M1 Area (%)	45.0	21.1	44.3	23.6	27.2	19.2	30.1	101.4
	M1 *f*	0.744	0.762	0.778	0.765	0.720	0.729	0.734	0.727
	M2a δ (mm/s)	1.14	1.15	1.13	1.15	1.18	1.17	1.17	
	M2a Δ (mm/s)	1.97	2.06	1.93	2.04	2.20	2.13	2.15	
	M2a Width (mm/s)	0.28	0.33	0.31	0.33	0.35	0.28	0.33	
	M2a Area (%)	55.0	78.9	55.7	76.4	30.5	25.7	31.5	
	M2a *f*	0.683	0.727	0.706	0.697	0.739	0.686	0.747	
	M2b δ (mm/s)					1.12	1.15	1.15	
	M2b Δ (mm/s)					1.80	1.84	1.84	
	M2b Width (mm/s)					0.31	0.34	0.32	
	M2b Area (%)					42.3	55.1	38.4	
	M2b *f*					0.8009	0.8071	0.8416	
80	M1 δ (mm/s)	1.31	1.30	1.30	1.30	1.30	1.30	1.30	1.32
	M1 Δ (mm/s)	3.13	3.06	3.06	3.04	3.09	3.03	3.05	2.77
	M1 Width (mm/s)	0.27	0.30	0.31	0.33	0.27	0.30	0.28	0.33
	M1 Area (%)	43.5	29.7	43.1	28.7	29.8	24.5	29.4	101.0
	M1 *f*	0.890	0.897	0.902	0.898	0.882	0.885	0.887	0.884
	M2a δ (mm/s)	1.27	1.27	1.26	1.27	1.30	1.30	1.30	
	M2a Δ (mm/s)	2.02	2.11	2.00	2.10	2.74	2.59	2.67	
	M2a Width (mm/s)	0.28	0.34	0.33	0.35	0.38	0.38	0.38	
	M2a Area (%)	56.5	70.3	56.9	71.3	32.8	35.9	45.3	
	M2a *f*	0.869	0.885	0.877	0.874	0.889	0.870	0.892	
	M2b δ (mm/s)					1.23	1.26	1.25	
	M2b Δ (mm/s)					1.84	1.97	1.91	
	M2b Width (mm/s)					0.31	0.33	0.32	
	M2b Area (%)					37.5	39.5	25.4	
	M2b *f*					0.910	0.912	0.924	
24	M1 δ (mm/s)	1.30	1.31	1.31	1.31	1.31	1.31		
	M1 Δ (mm/s)	3.13	3.05	3.06	3.02	3.09	3.05		
	M1 Width (mm/s)	0.57	0.34	0.33	0.36	0.30	0.37		
	M1 Area (%)	56.7	28.5	42.4	28.5	28.7	16.2		
	M1 *f*	0.9110	0.9154	0.9187	0.9160	0.9060	0.9084		
	M2a δ (mm/s)	1.26	1.28	1.27	1.28	1.31	1.31		
	M2a Δ (mm/s)	2.05	2.13	2.02	2.11	2.71	2.54		
	M2a Width (mm/s)	0.54	0.35	0.35	0.37	0.43	0.47		
	M2a Area (%)	43.3	71.5	57.6	71.5	34.7	48.2		
	M2a *f*	0.8990	0.9080	0.9035	0.9019	0.9110	0.8996		
	M2b δ (mm/s)					1.24	1.26		
	M2b Δ (mm/s)					1.84	1.97		
	M2b Width (mm/s)					0.32	0.35		
	M2b Area (%)					36.6	35.6		
	M2b *f*					0.9240	0.9253		

Center shift (δ) expressed relative to the midpoint of Fe foil. Δ = quadrupole splitting, and width is expressed as full width at half peak maximum. Area given as percentage of the total spectral area assigned to that doublet. *f* = recoil-free fraction.

FIGURES AND FIGURE CAPTIONS

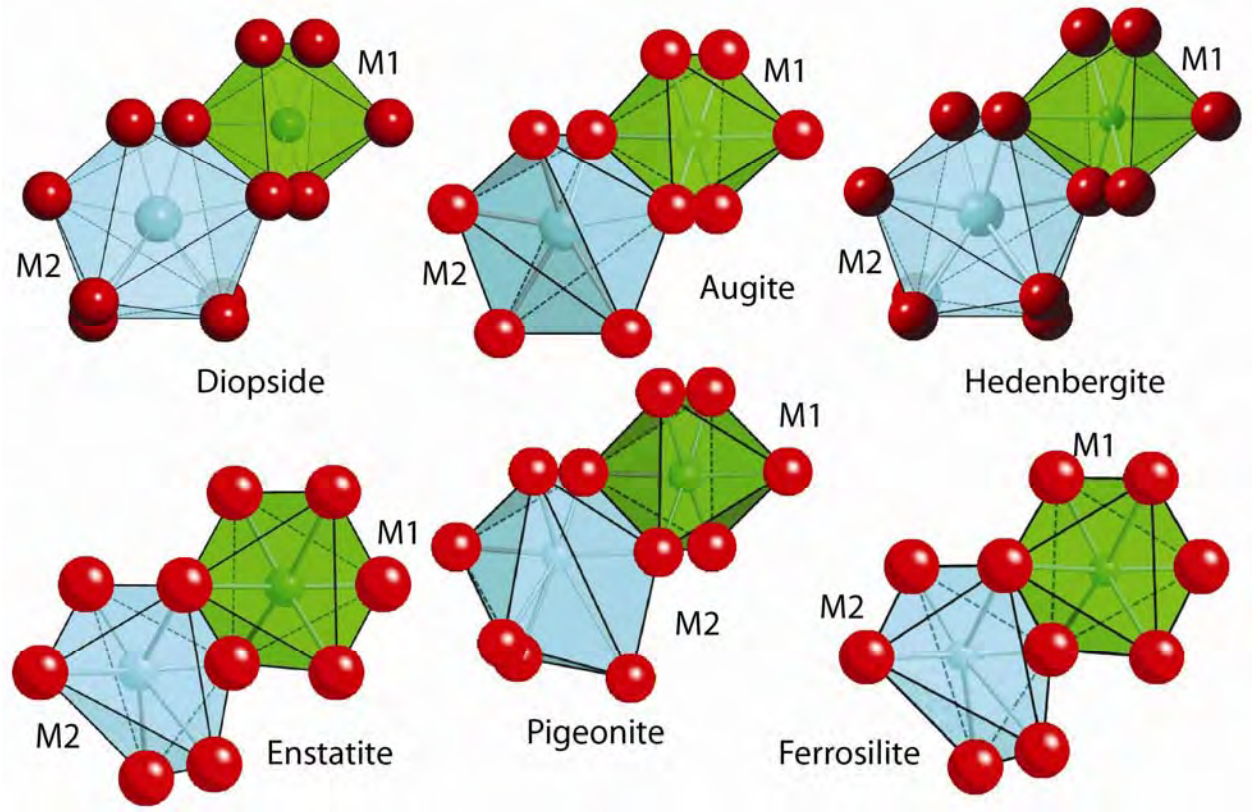

Figure 1. View down the *a* axis of different pyroxenes distributed across the Ca-Mg-Fe quadrilateral, illustrating variations in average geometry of the M1 and M2 sites in pyroxene as a function of space group and composition. In typical rock-forming parageneses, pyroxenes along the Mg-Fe join are orthopyroxenes, while those above this line are clinopyroxenes. Enstatite structure is from Hugh-Jones et al. (1994), ferrosilite from Sueno et al. (1976), pigeonite from Brown et al. (1972), augite from Bertolo et al. (1994), diopside from Cameron et al. (1973), and hedenbergite from Zhang et al. (1997).

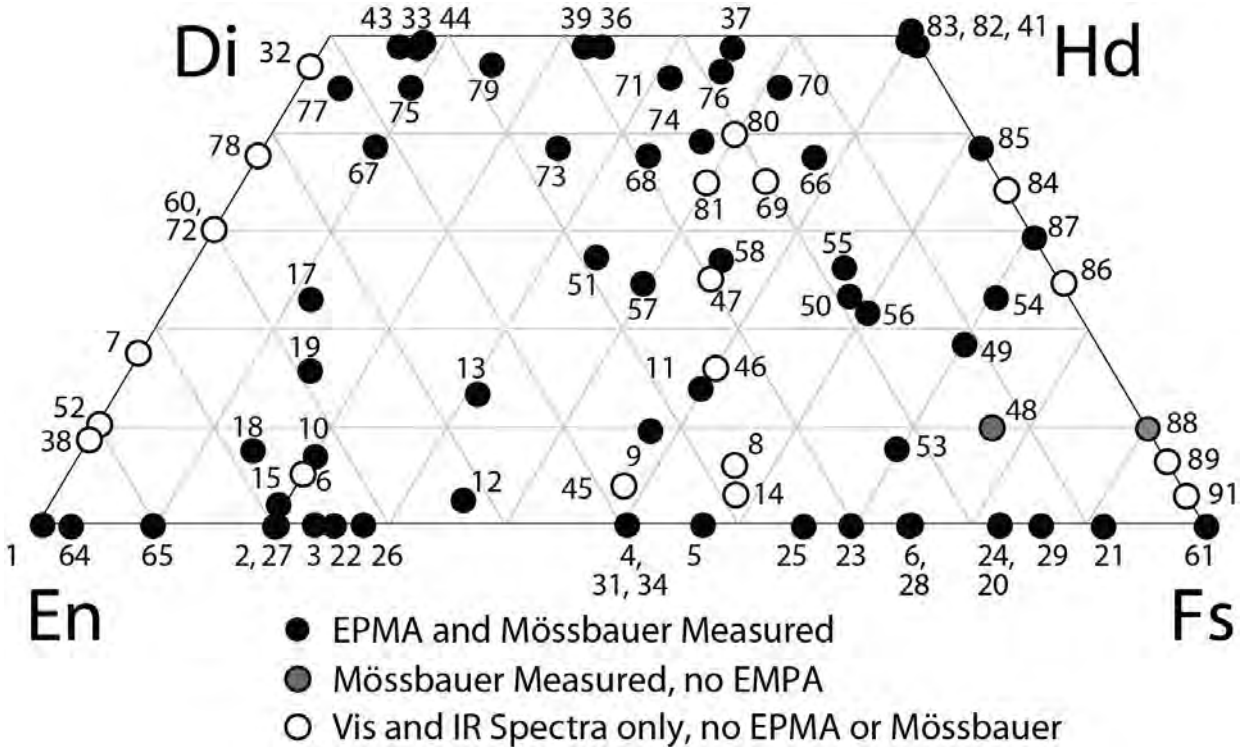

Figure 2. Compositions in this suite of synthetic samples plotted on the Ca-Mg-Fe quadrilateral. Black circles represent samples for which both Mössbauer and electron microprobe data were acquired. Gray circles are ones for which probe data were not obtained, and outlines circles are samples for which only vis-IR spectra were obtained (see Klima et al. 2010).

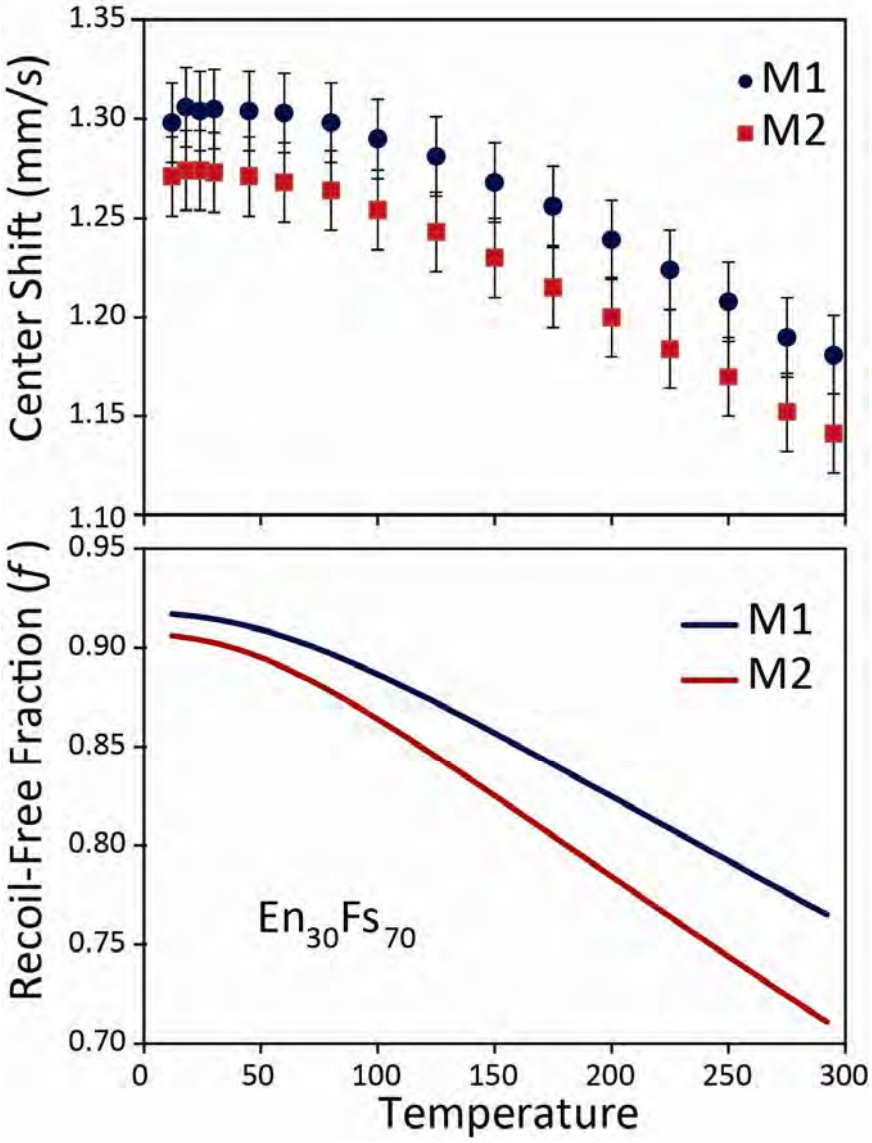

Figure 3. Example models showing the basis for calculation of recoil-free fraction using the change in center shift as a function of temperature for sample px023 ($En_{30}Fs_{70}$). Top panel shows the change in center shift with temperature fit by the model in Equations 5 and 6, while the bottom panel shows the modeled value of *f* for that data series.

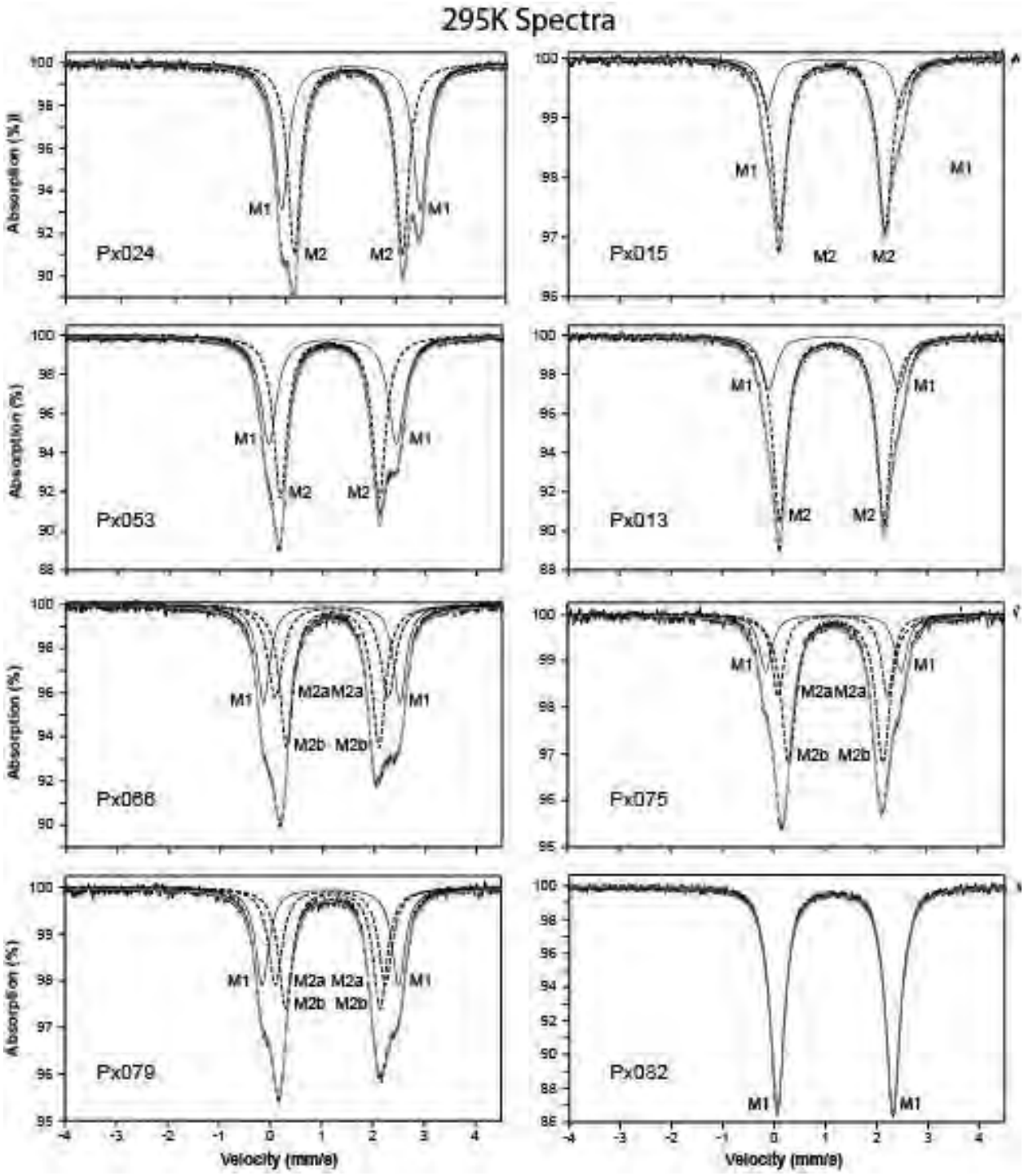

722

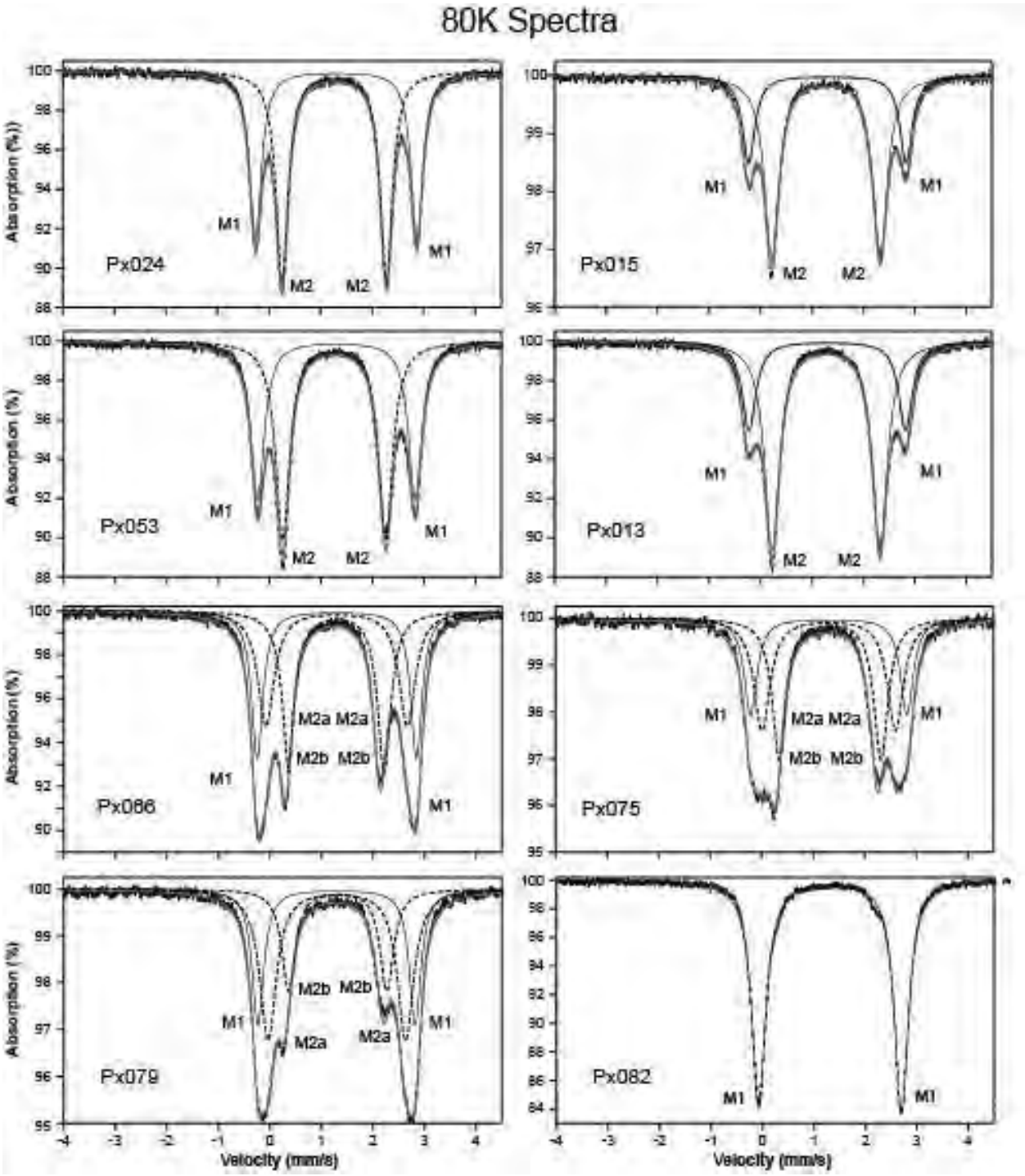

Figure 4a,b. Fitted Mössbauer spectra of eight pyroxenes from Table 2, acquired at 295K and 80K. The outer M1 doublet is shown as a solid line, while inner M2 doublets (in some cases, two M2 doublets representing different local corrdination polyhedral arbitrarily designated as M2a and M2b following historical precedent) are shown as dashed lines. The envelope of all fitted peaks in each plot is shown in gray.

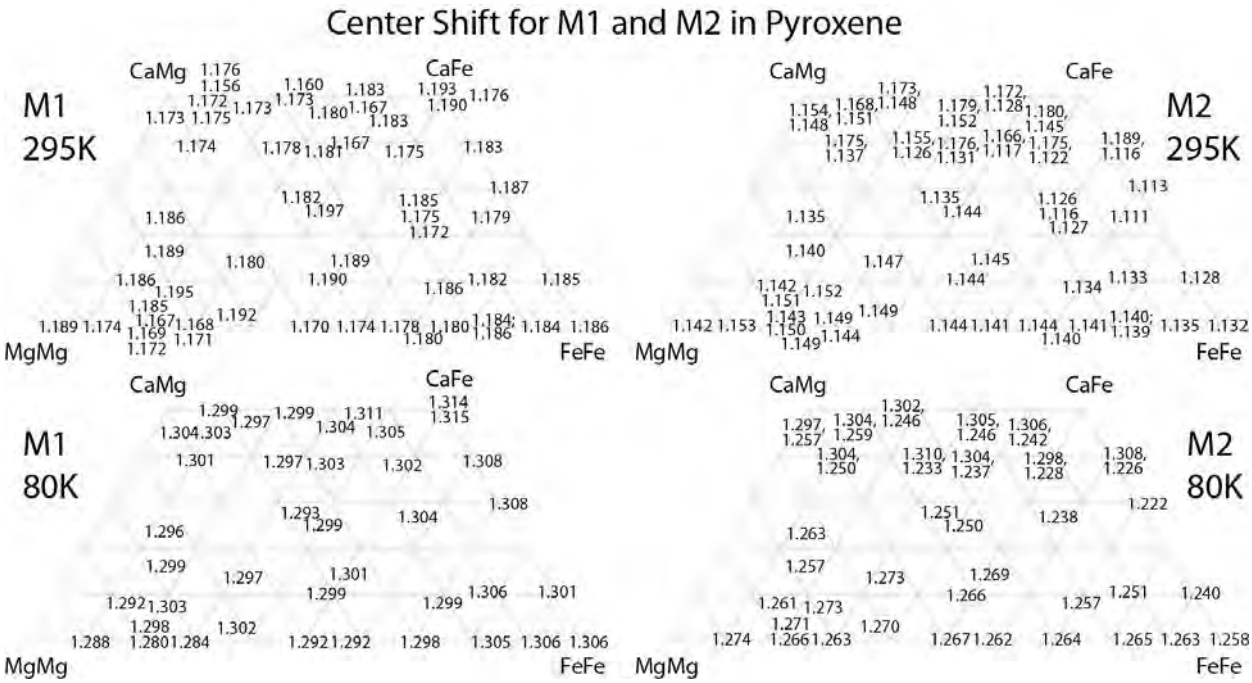

Figure 5. Observed center shift (δ) for Fe^{2+} doublets in M1 (left) and M2 (right) sites at 295K (top) and 80K (bottom). Positions of values have been moved slightly for legibility; see Table 3 for exact values.

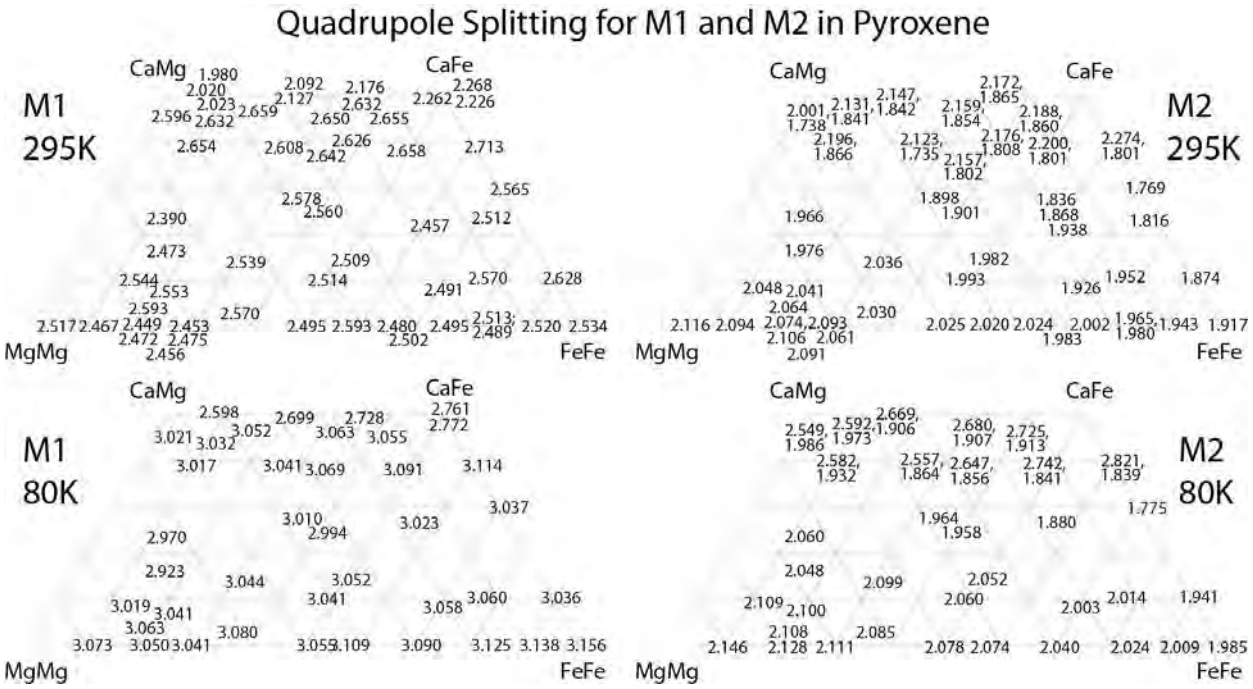

Figure 6. Observed values for quadrupole splitting for Fe^{2+} doublets in M1 (left) and M2 (right) sites at 295K (top) and 80K (bottom). Positions of values have been moved slightly for legibility; see Table 3 for exact values.

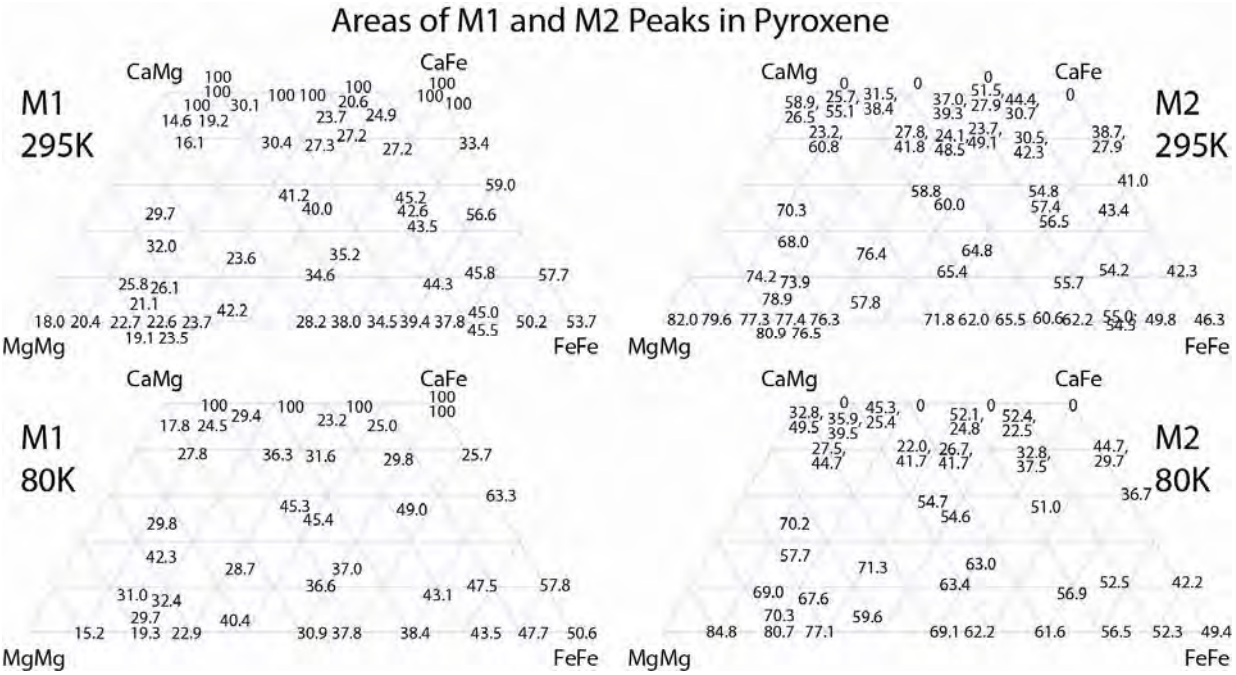

Figure 7. Observed areas (%) of the fraction of total spectral area in Fe^{2+} doublets in M1 (left) and M2 (right) sites at 295K (top) and 80K (bottom). Positions of values have been moved slightly for legibility; see Table 3 for exact values.

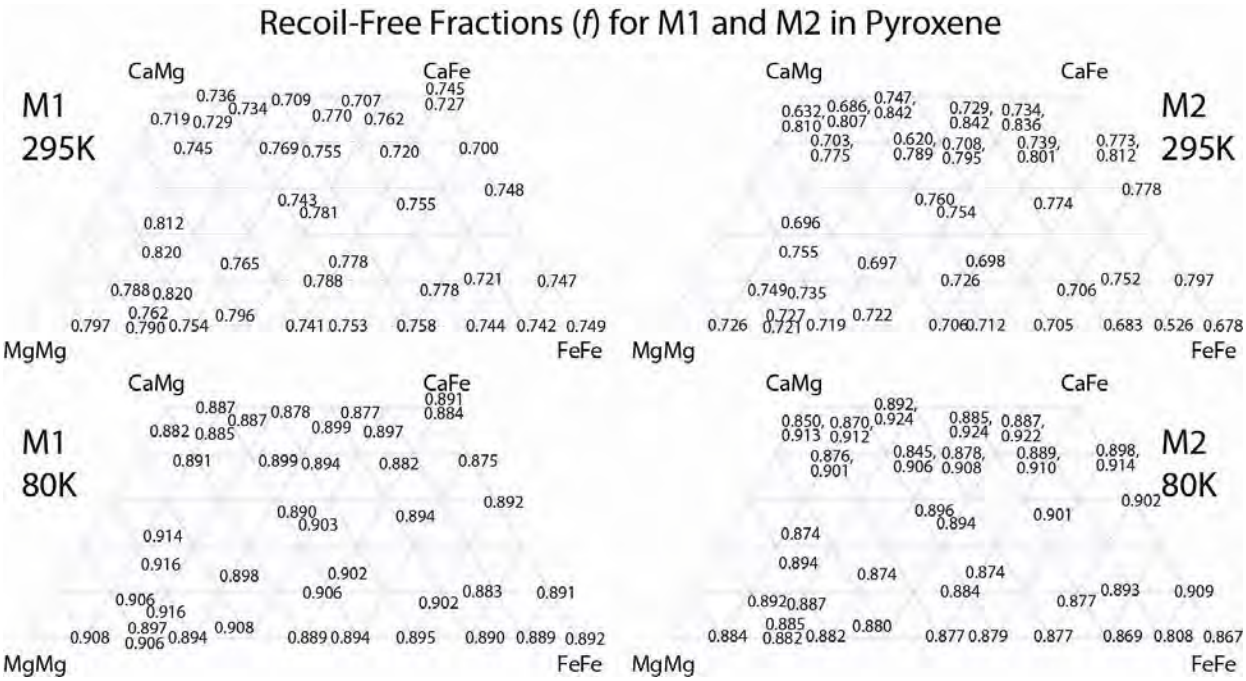

Figure 8. Modeled recoil-free fraction values for Fe^{2+} doublets in M1 (left) and M2 (right) sites at 295K (top) and 80K (bottom). Positions of values have been moved slightly for legibility; see Table 3 for exact values.

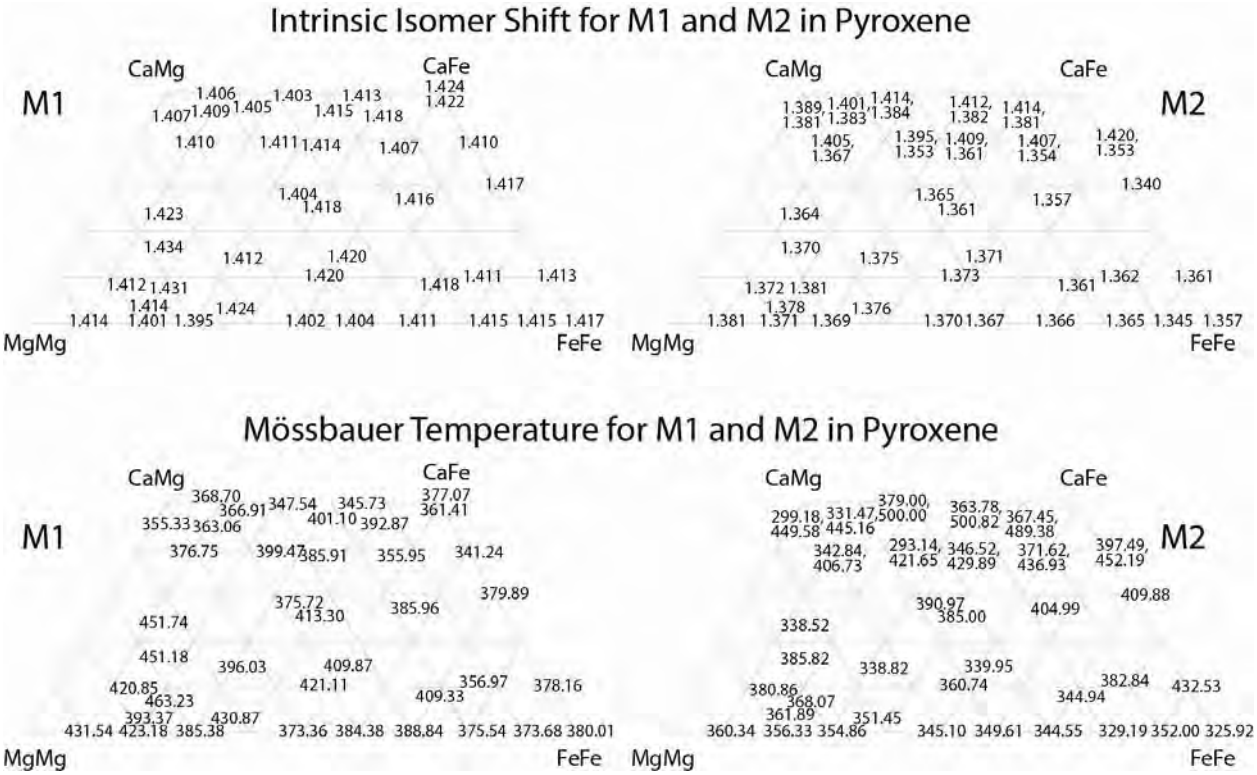

Figure 9. Calculated values of intrinsic isomer shift (top) and Mössbauer temperature (bottom) for Fe^{2+} doublets in M1 (left) and M2 (right) sites at 295K (top) and 80K (bottom). Positions of values have been moved slightly for legibility; see Table 3 for exact values.

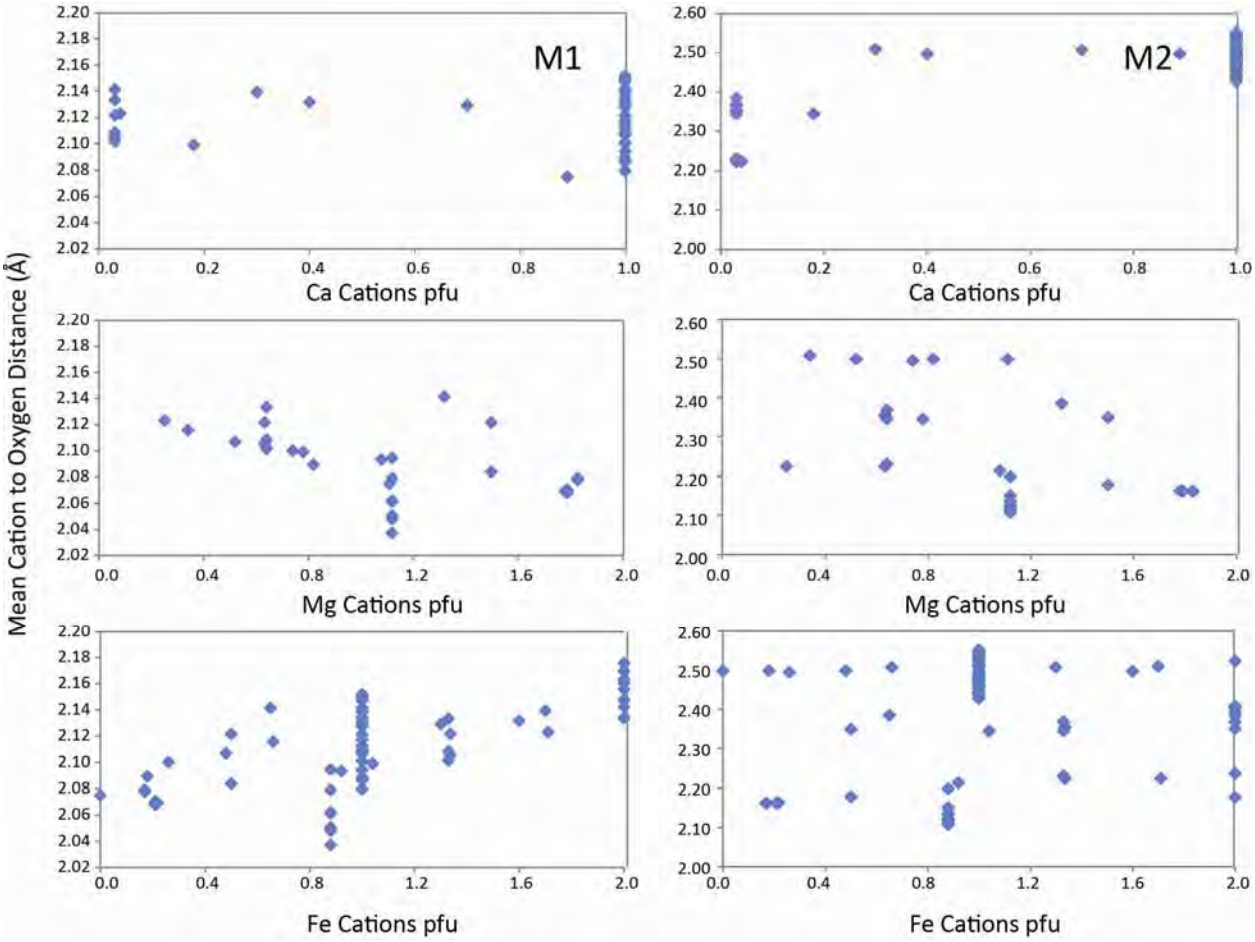

Figure 10. Mean cation to oxygen bond distance as a function of composition for Ca-Mg-Fe pyroxenes. Values based upon calculations using data from Freed and Peacor (1967), Clark and Papike (1968), Morimoto and Guven (1970), Burnham et al. (1971), Clark et al. (1971), Cameron et al. (1973), Smyth (1973), Ohashi et al. (1975), Sueno et al. (1976), Molin (1989), Angel et al. (1989), Raudsepp et al. (1990), Hazen et al. (1993), Hugh-Jones and Angel (1994), Hugh-Jones et al. (1994), Yang and Ghose (1995), Harlow (1996), Zhang et al. (1997), Heuer et al. (2005), and Nestola et al. (2008). The M1 site is most affected by variations in Fe and Mg, while the M2 site is predominantly influenced by changes in Ca content. Error bars are the same size or smaller as the symbols used.

773

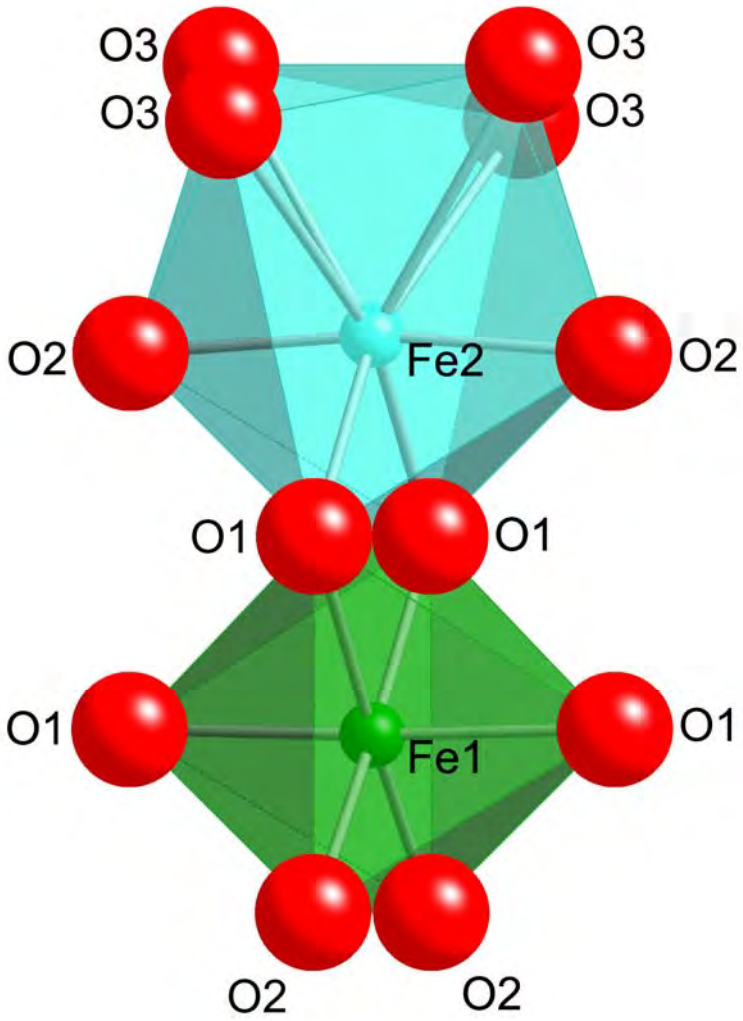

774
775 Figure 11. View down the *x* axis of a $Fs_{80}Wo_{20}$ pyroxene based on coordinates from Ohashi et
776 al. (1975), showing names and locations of oxygen atoms surrounding the Fe cations in the M1
777 and M2 sites. The *z* axis is horizontal and the *y* axis is vertical.

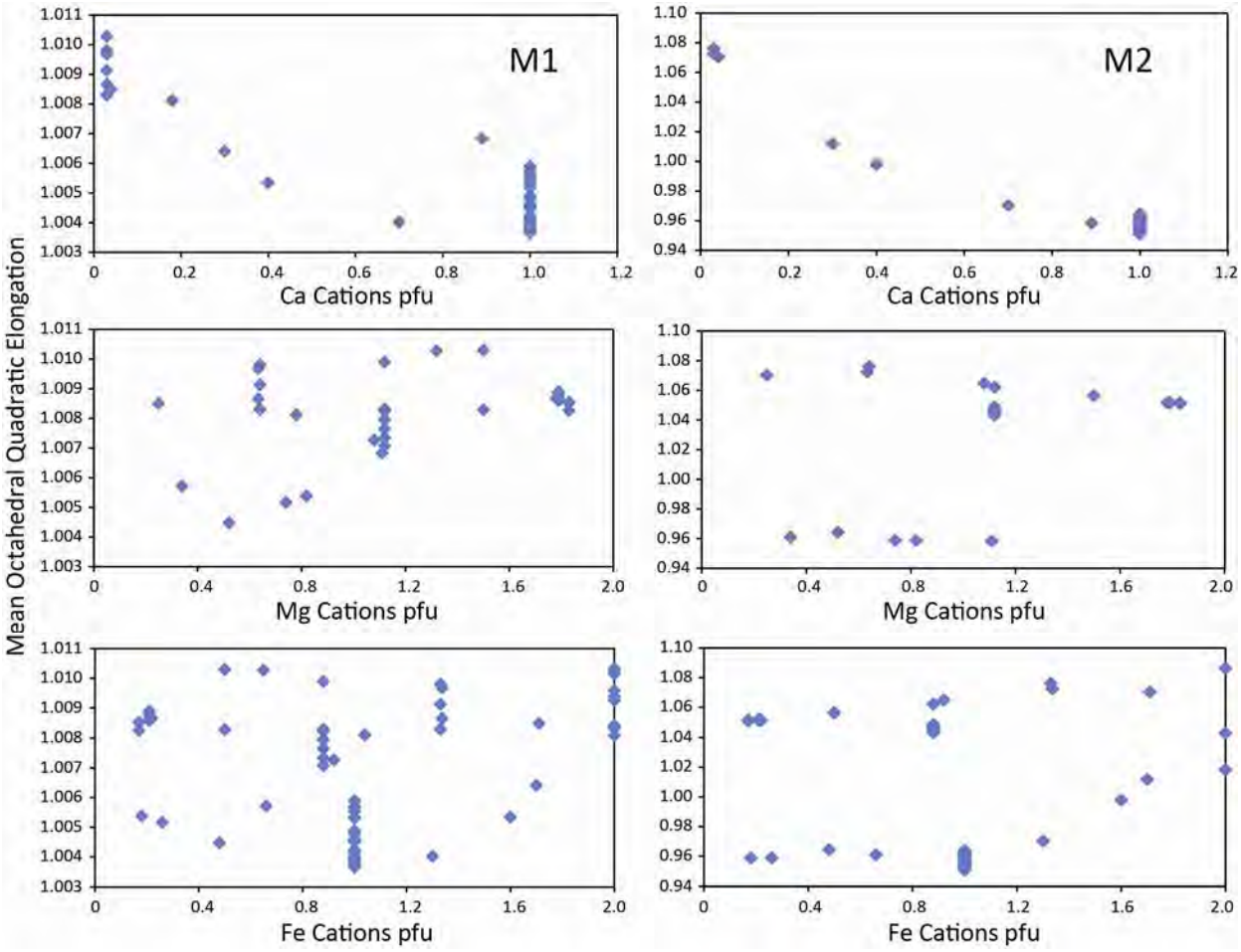

Figure 12. Mean quadratic elongation (from Robinson et al. 1971) plotted against cation composition The effect of increasing Ca substitution is to reduce the mean elongation of both the M1 and M2 sites. Error bars are the same size as or smaller than the symbols used.

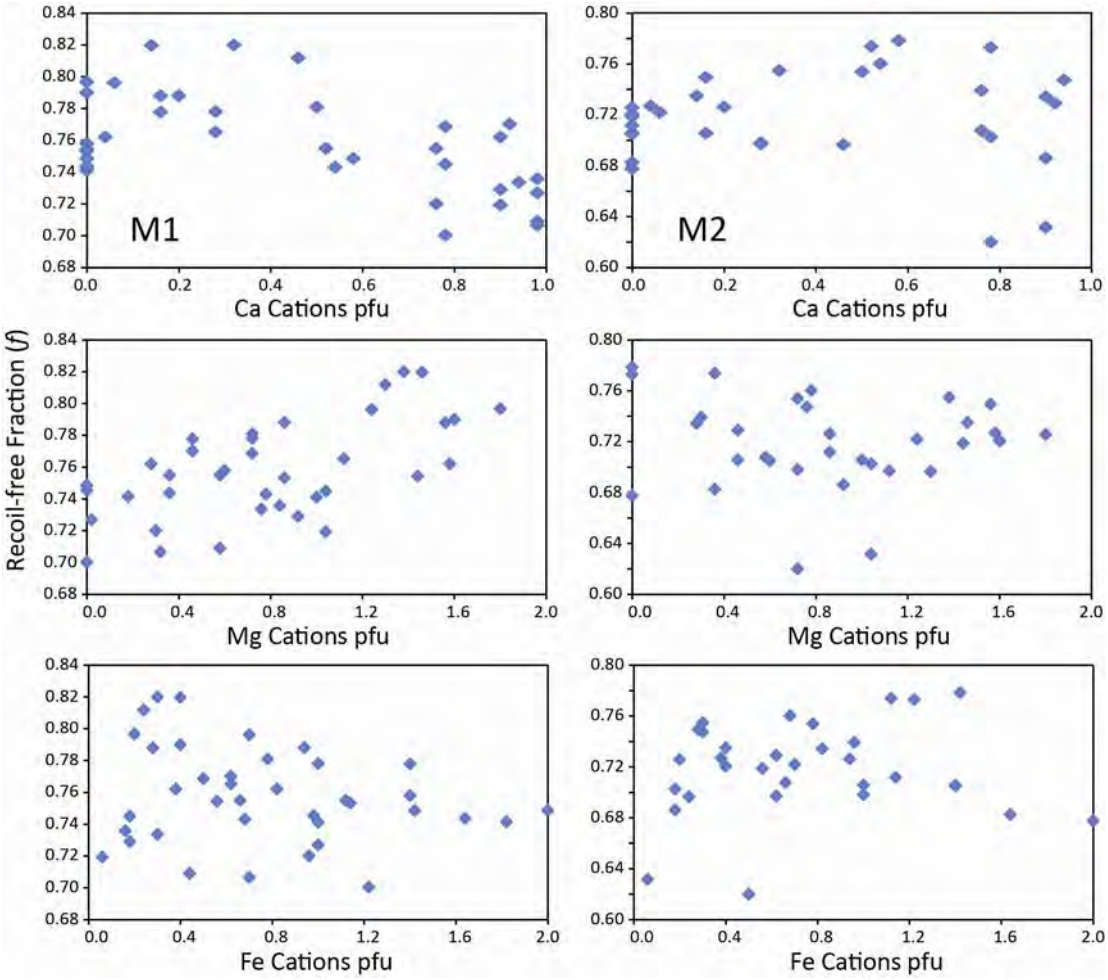

Figure 13. Relationship between recoil-free fraction (*f*) and cation substitution in synthetic pyroxenes from Figures 10 and 11. Error bars are the same size as or smaller than the symbols used.

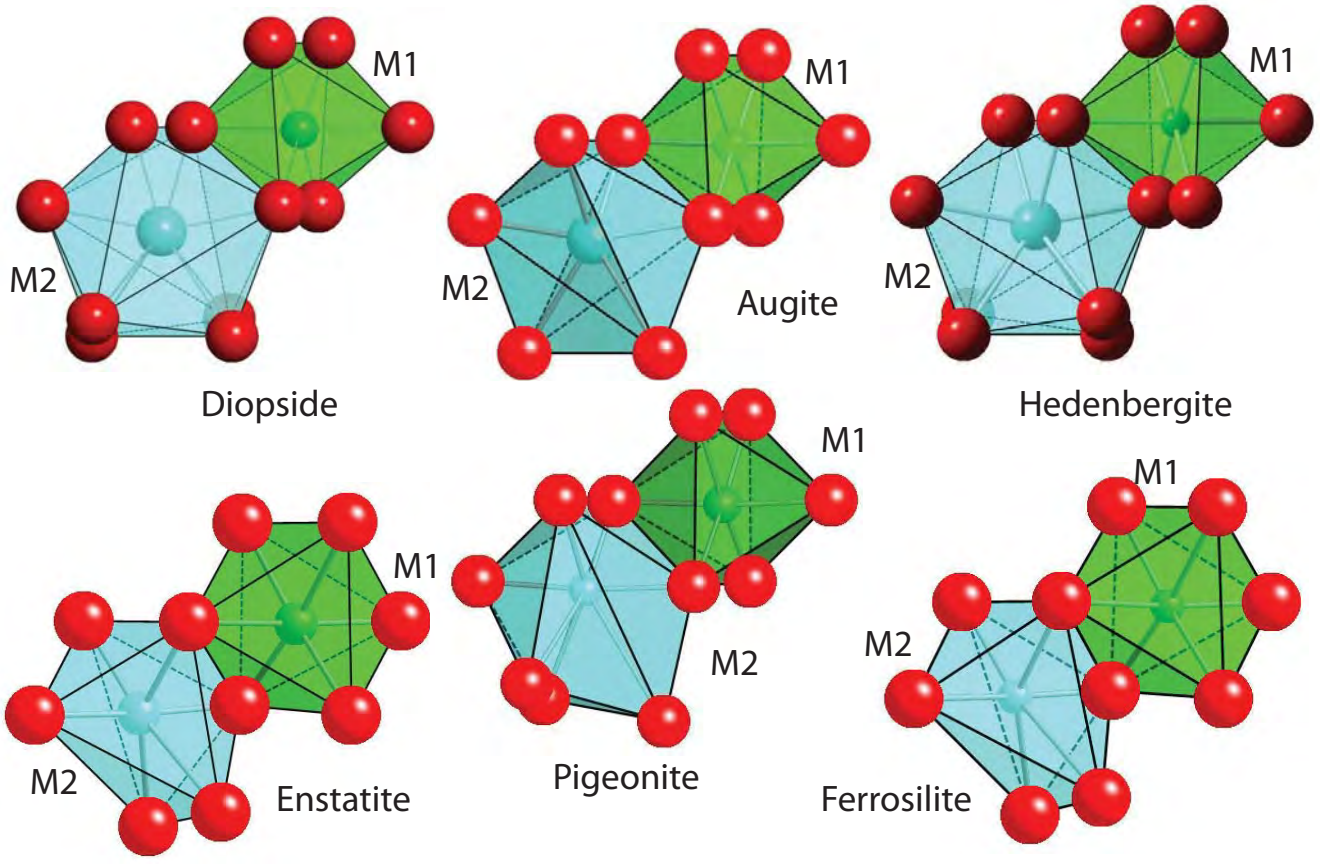
M1
M2
Diopside
M1
M2
Augite
M1
M2
Hedenbergite
M1
M2
Enstatite
M1
M2
Pigeonite
M1
M2
Ferrosilite

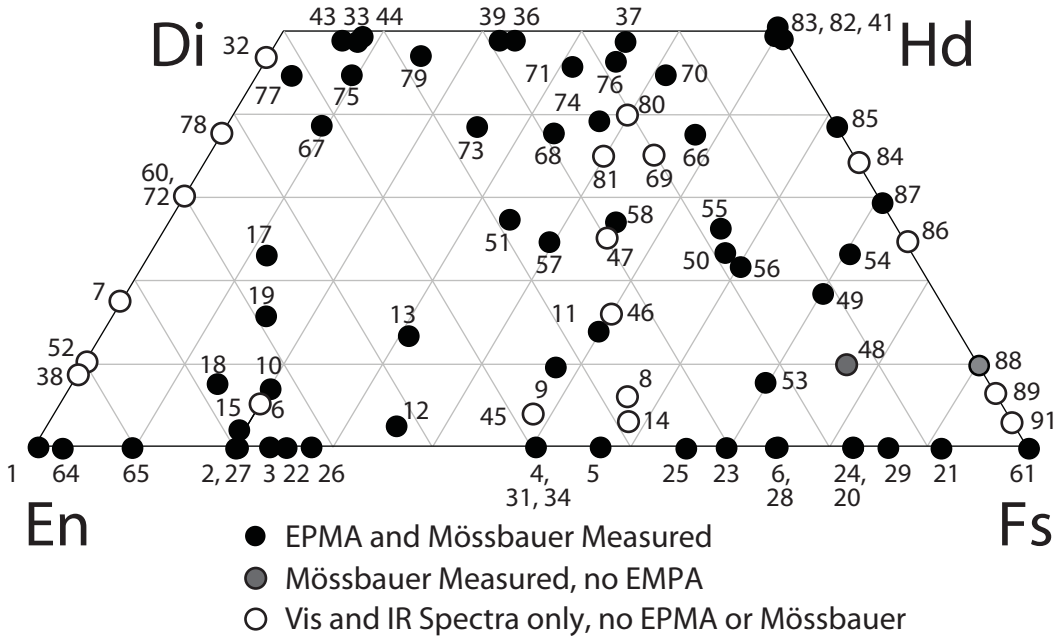
Di
Hd
En
Fs
43 33 44
39 36
37
83, 82, 41
32
79
71
76
70
77
75
74
80
78
67
73
68
81
69
66
85
84
60,
72
87
58
55
86
17
51
57
47
50
56
54
7
19
13
11
46
49
52
48
38
18
10
9
8
53
88
89
15
6
12
45
14
91
1
64
65
2, 27
3
22
26
4,
31, 34
5
25
23
6,
28
24,
20
29
21
61
EPMA and Mössbauer Measured
Mössbauer Measured, no EMPA
Vis and IR Spectra only, no EPMA or Mössbauer

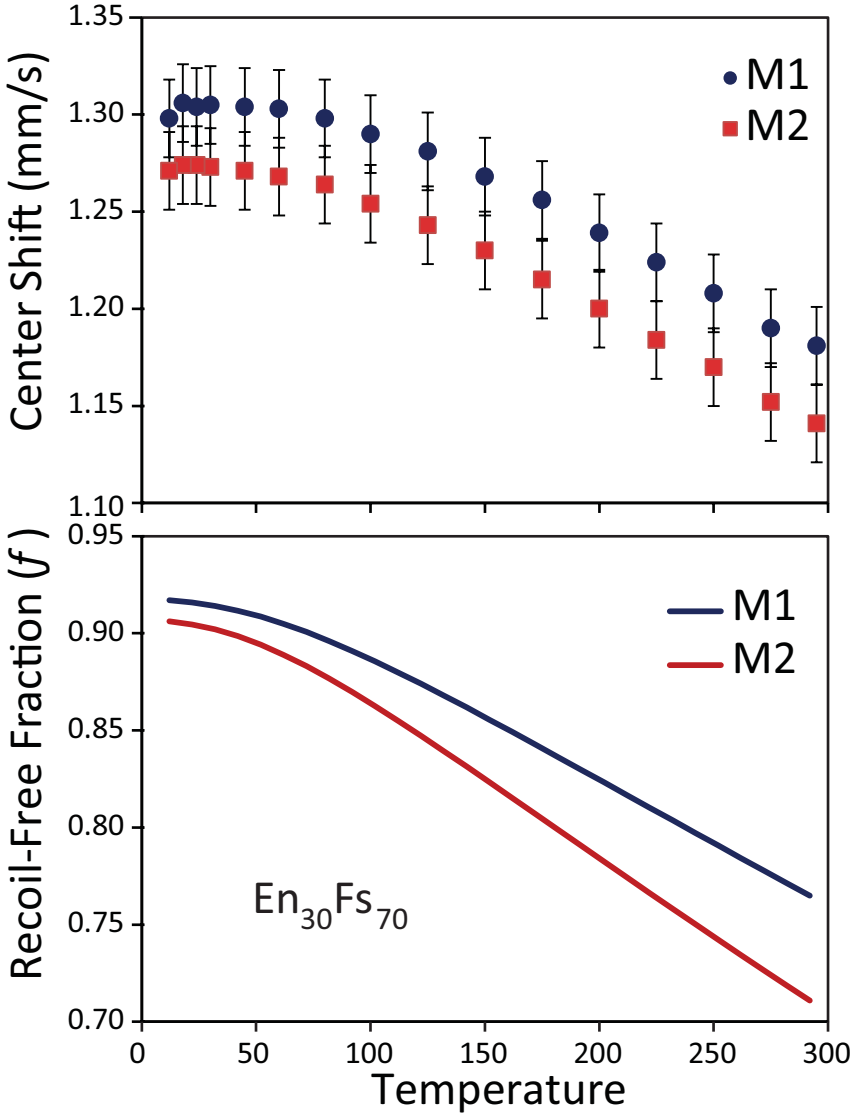
Center Shift (mm/s)
1.35
1.30
1.25
1.20
1.15
1.10
M1
M2
Recoil-Free Fraction (f)
0.95
0.90
0.85
0.80
0.75
0.70
M1
M2
En30Fs70
0
50
100
150
200
250
300
Temperature

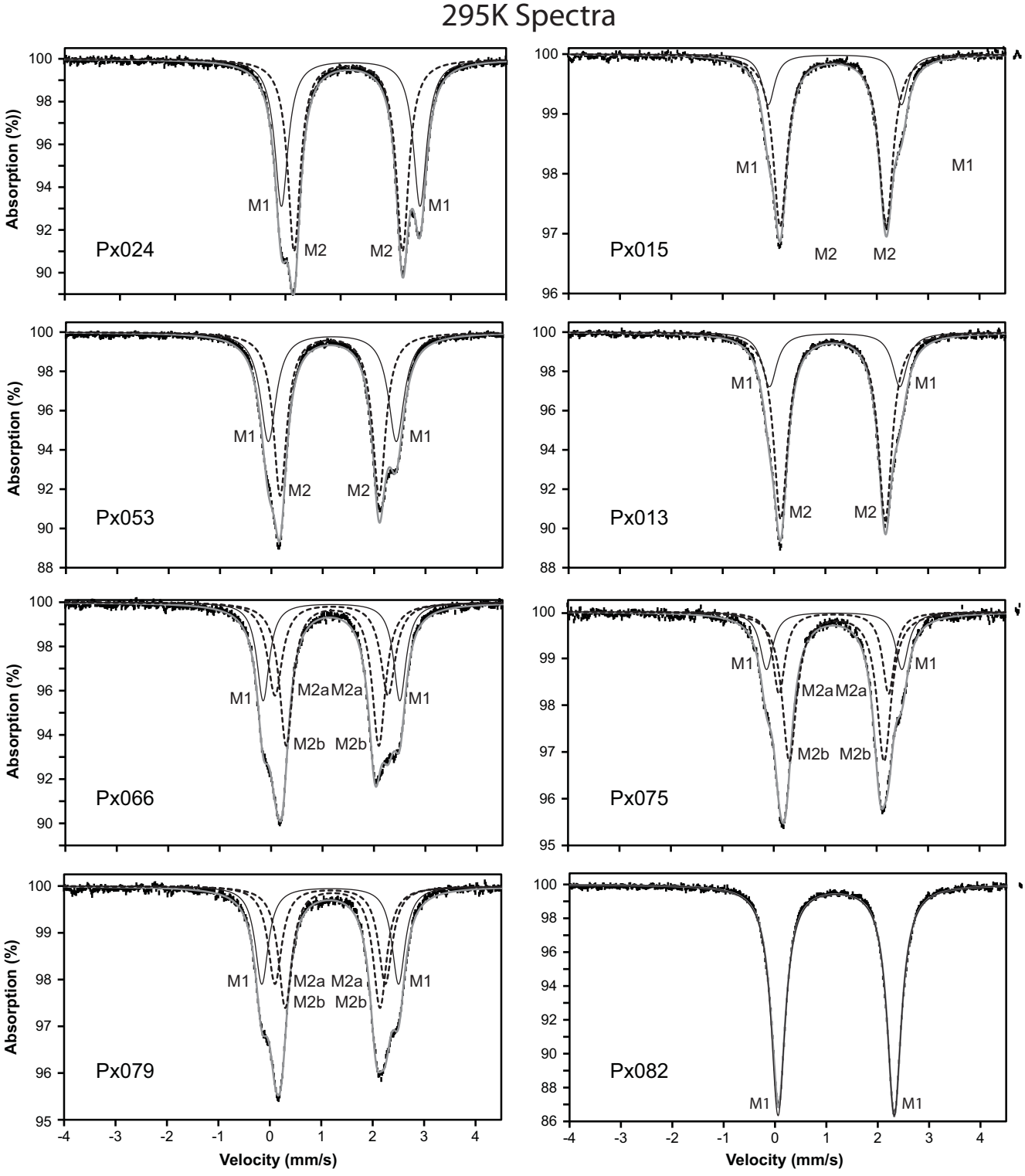
295K Spectra
Absorption (%))
Absorption (%)
Velocity (mm/s)
Px024
Px015
Px053
Px013
Px066
Px075
Px079
Px082
M1
M2
M2a
M2b

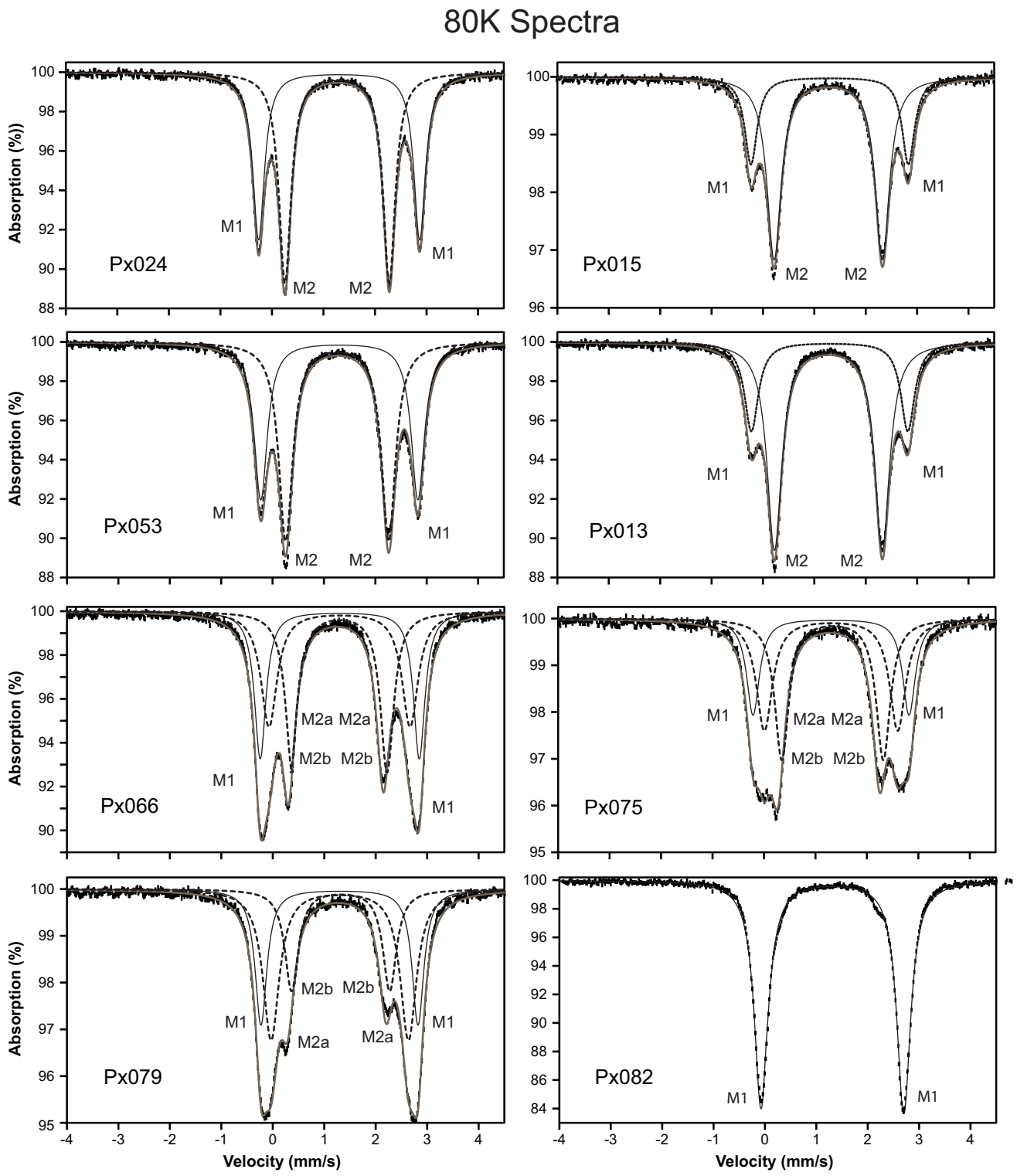
80K Spectra
Absorption (%))
Absorption (%)
Velocity (mm/s)
Px024
Px015
Px053
Px013
Px066
Px075
Px079
Px082
M1
M2
M2a
M2b

Center Shift for M1 and M2 in Pyroxene

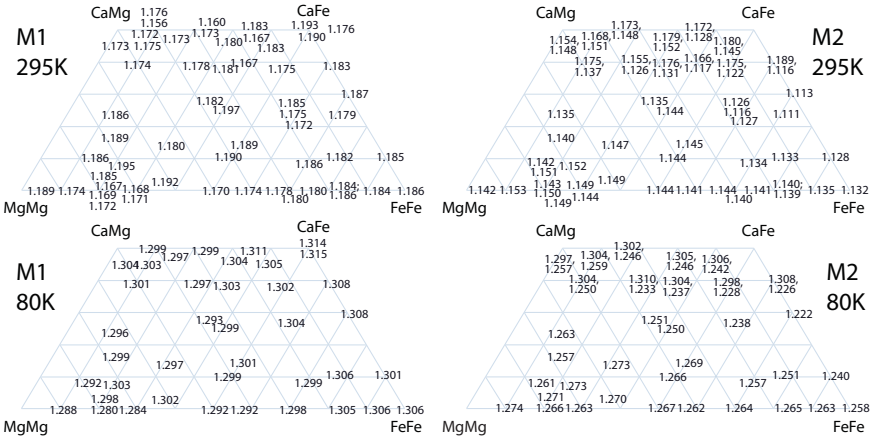

Quadrupole Splitting for M1 and M2 in Pyroxene

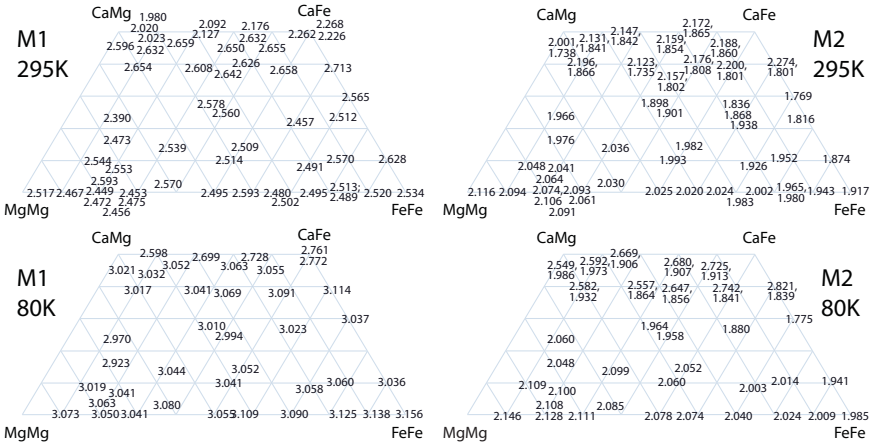

Areas of M1 and M2 Peaks in Pyroxene

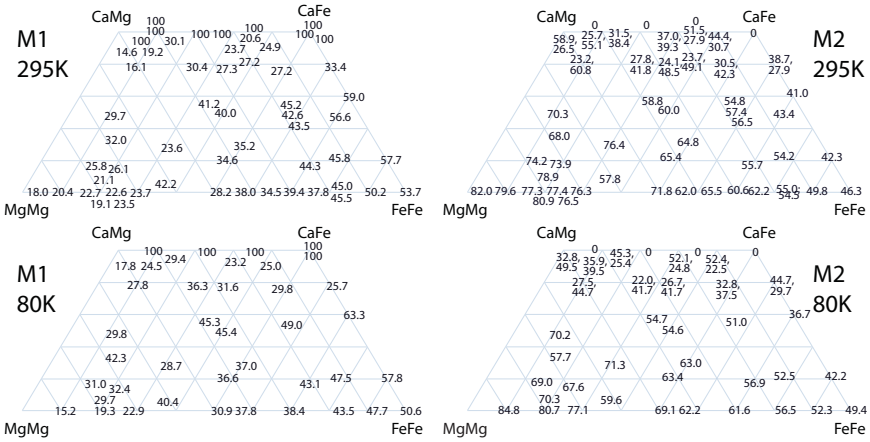

Recoil-Free Fractions (*f*) for M1 and M2 in Pyroxene

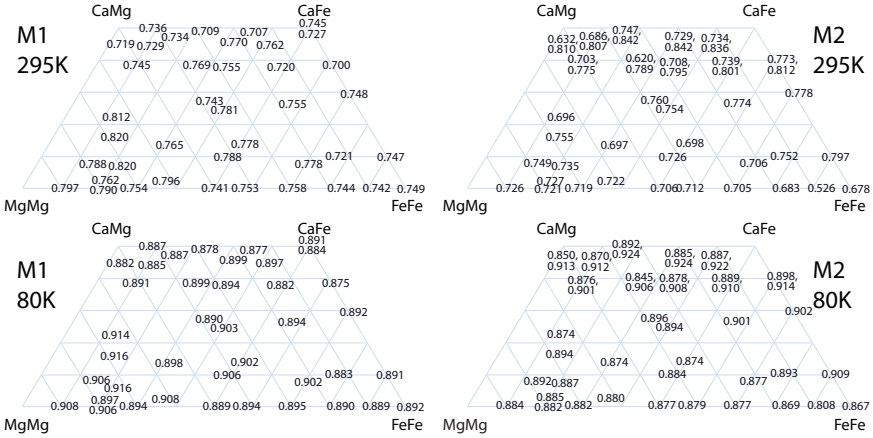

Intrinsic Isomer Shift for M1 and M2 in Pyroxene

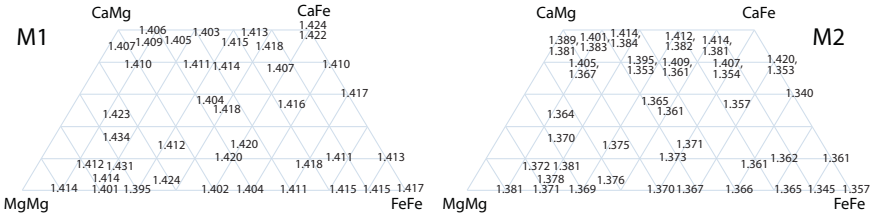

Mössbauer Temperature for M1 and M2 in Pyroxene

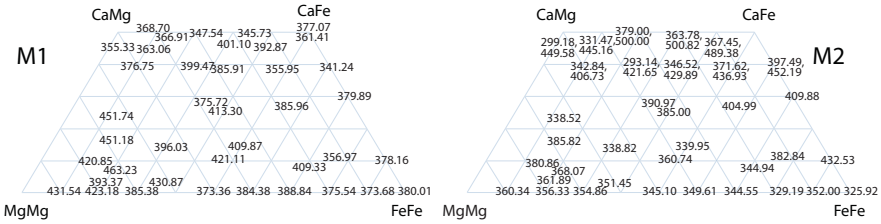

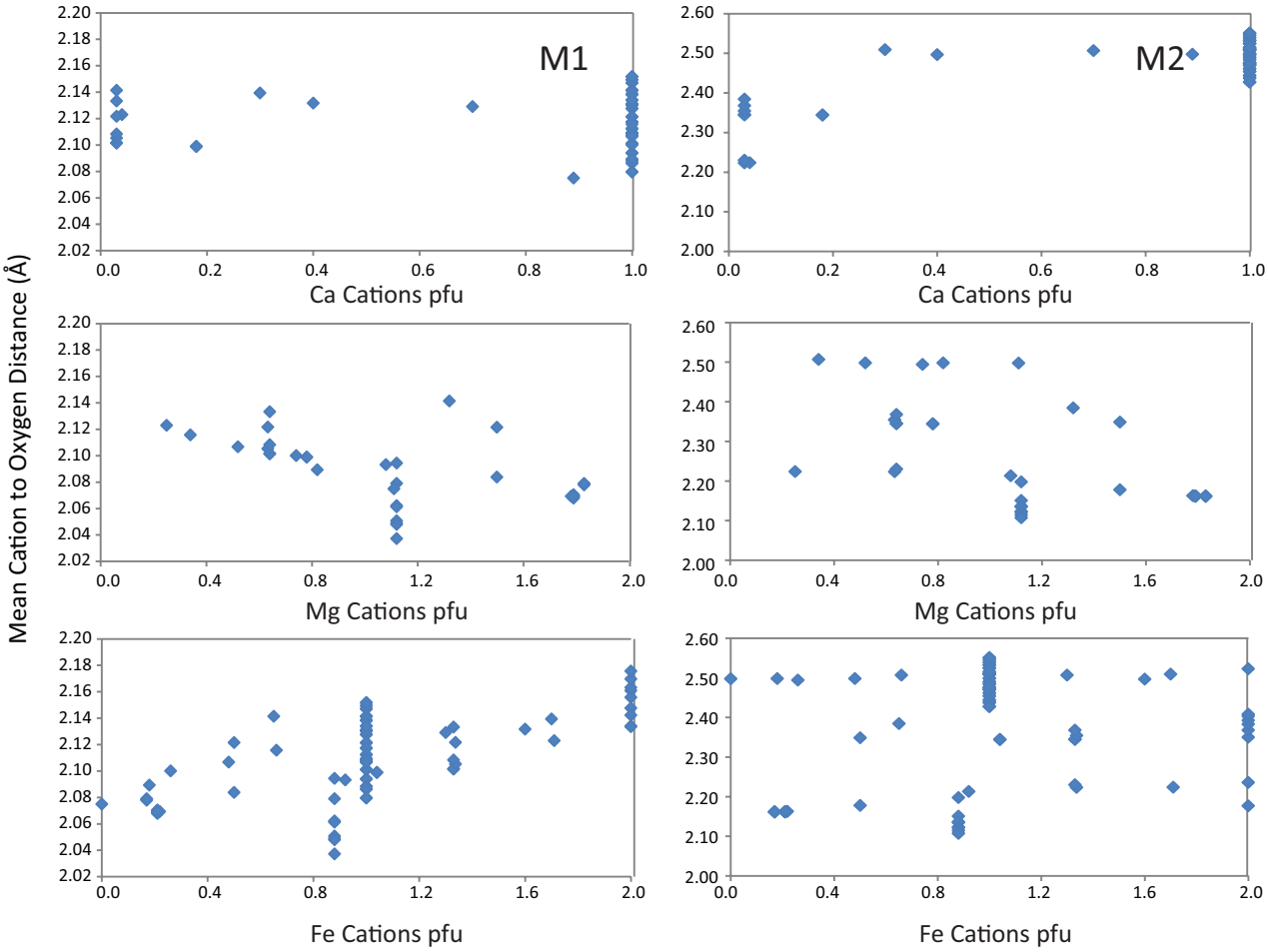
M1
M2
Mean Cation to Oxygen Distance (Å)
Ca Cations pfu
Mg Cations pfu
Fe Cations pfu

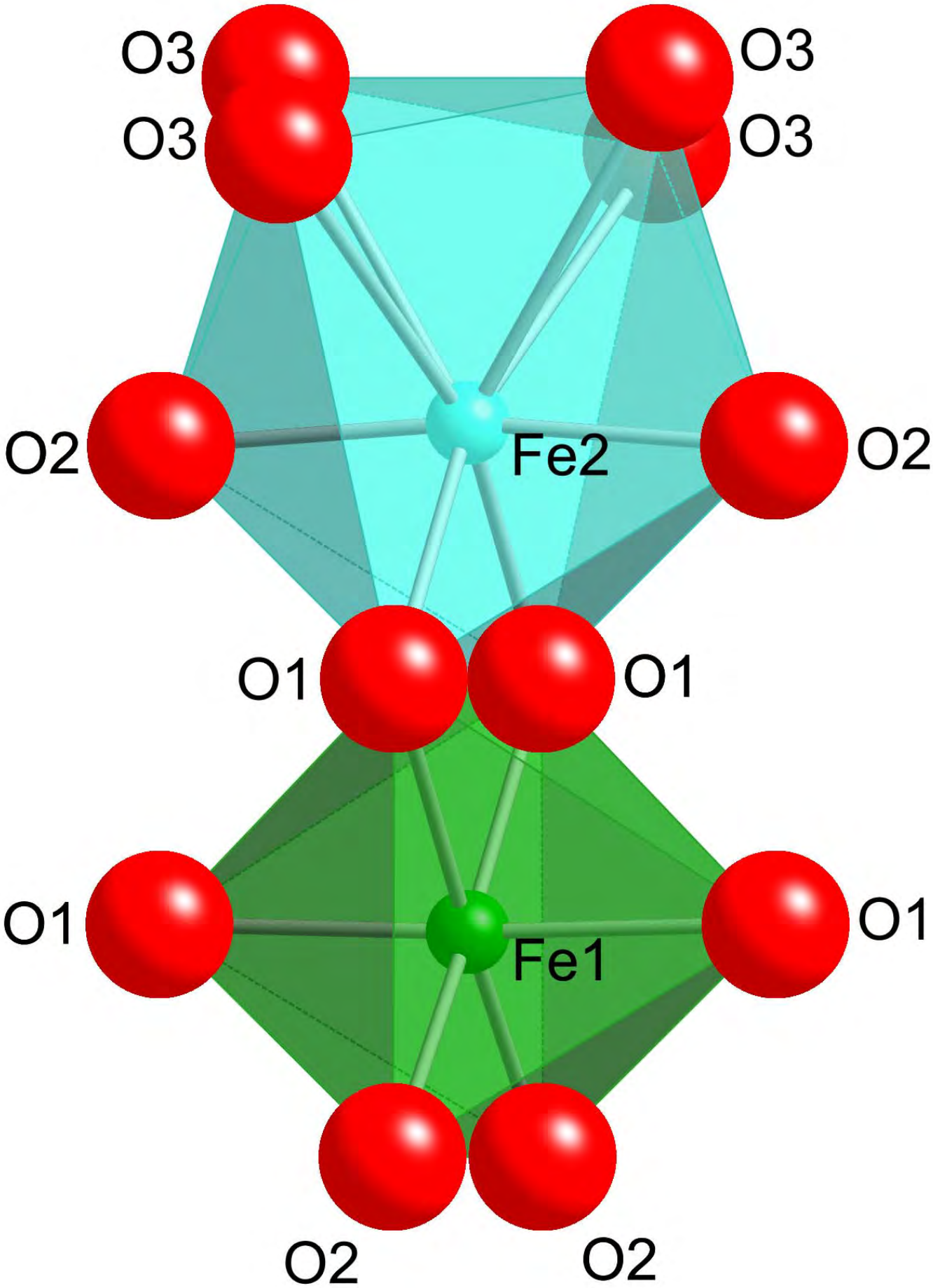
O3
O3
O3
O3
O2
Fe2
O2
O1
O1
O1
Fe1
O1
O2
O2

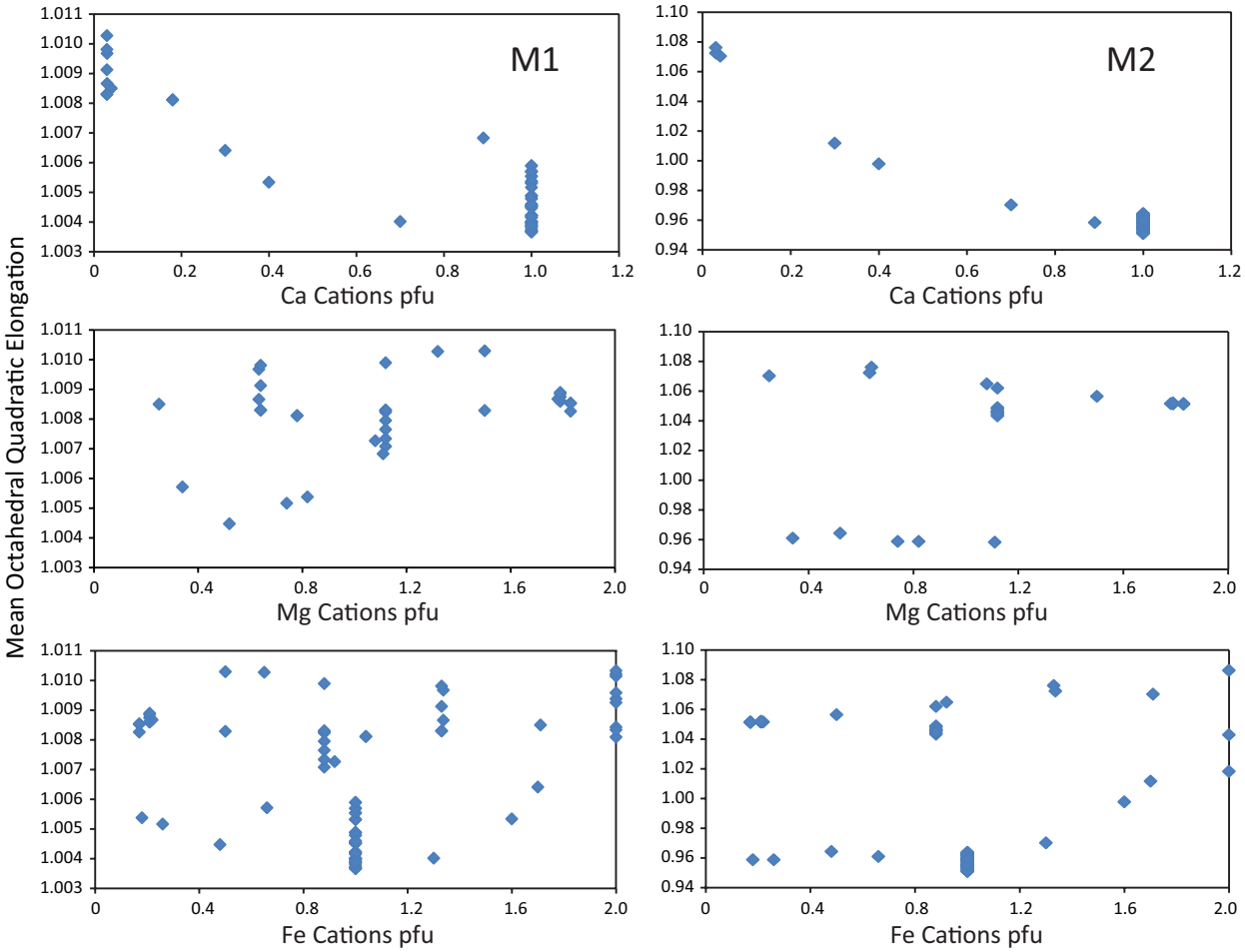
M1
M2
Mean Octahedral Quadratic Elongation
Ca Cations pfu
Mg Cations pfu
Fe Cations pfu

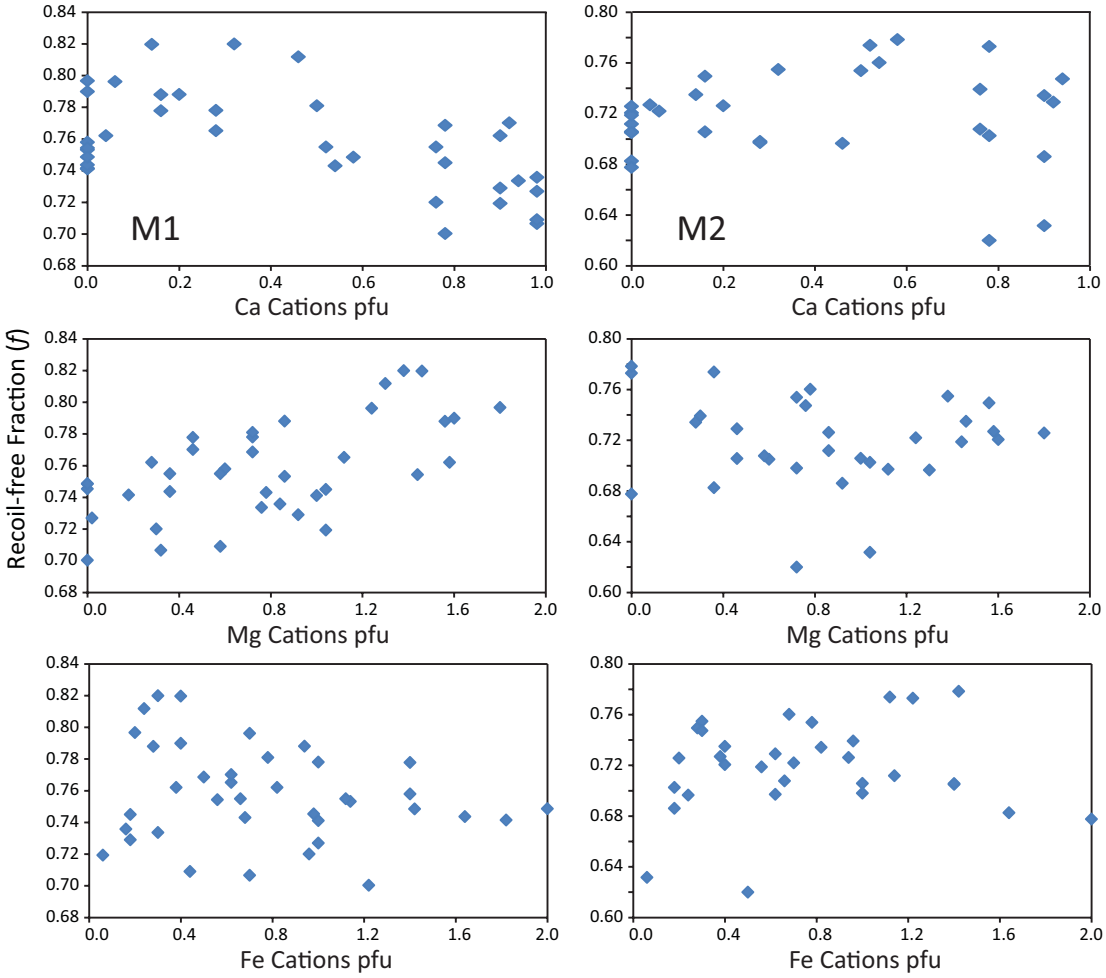
M1
M2
Recoil-free Fraction (f)
Ca Cations pfu
Mg Cations pfu
Fe Cations pfu